iScience

CellPress
OPEN ACCESS

Article

Rapid Processing and Drug Evaluation in Glioblastoma Patient-Derived Organoid Models with 4D Bioprinted Arrays

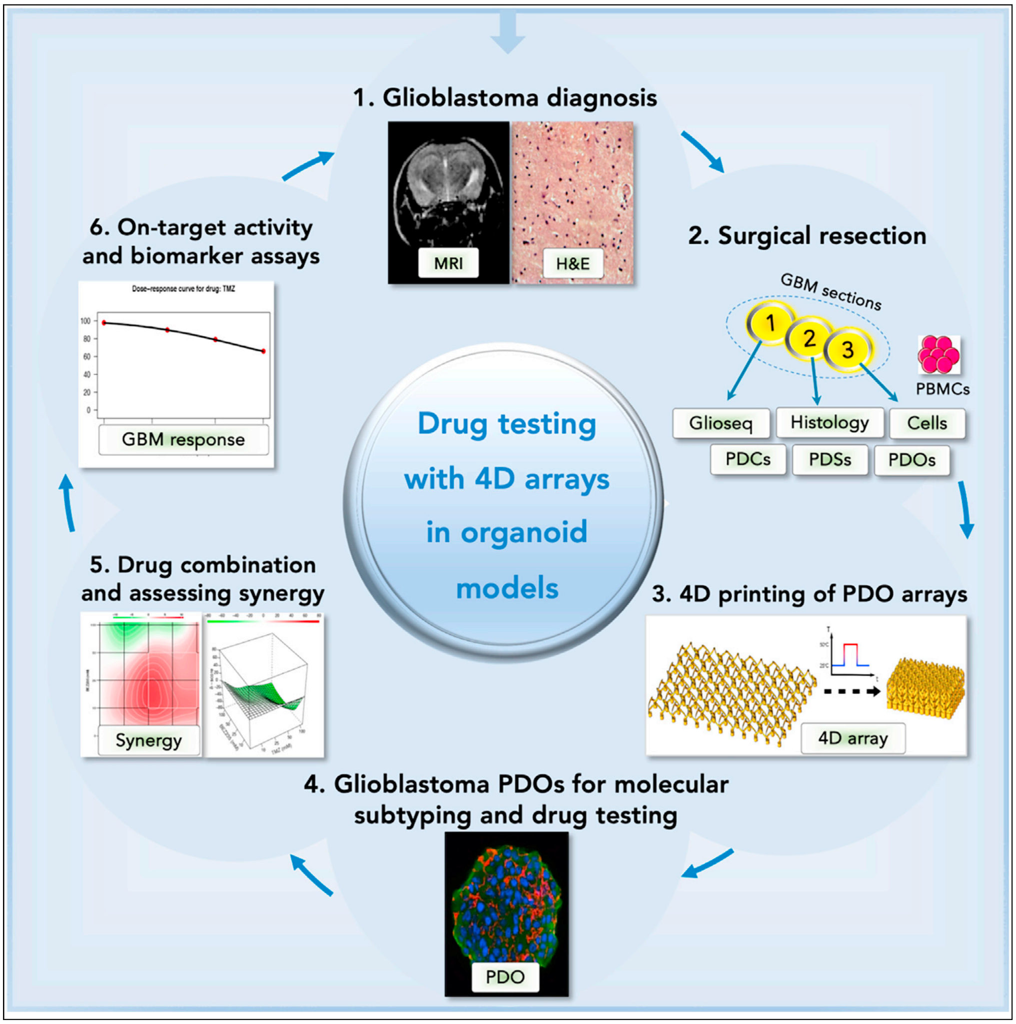

Michelle Chadwick, Chen Yang, Liqiong Liu, Christian Moya Gamboa, Kelly Jara, Howon Lee, Hatem E. Sabaawy

howon.lee@rutgers.edu (H.L.)
sabaawhe@cinj.rutgers.edu (H.E.S.)

HIGHLIGHTS

4D printed thermo-responsive polymer arrays self-transform for 3D culture and histology

Patient-derived organoid models represent original tumors better than spheres in arrays

Cellular heterogeneity and drug responses are assessed in glioblastoma organoid models

Functional utility is shown by detecting drug sensitivity, on-target activity, and synergy

Chadwick et al., iScience *23*, 101365
August 21, 2020 © 2020
https://doi.org/10.1016/j.isci.2020.101365

iScience

CellPress
OPEN ACCESS

Article

Rapid Processing and Drug Evaluation in Glioblastoma Patient-Derived Organoid Models with 4D Bioprinted Arrays

Michelle Chadwick,[1,4] Chen Yang,[2,4] Liqiong Liu,[1,4] Christian Moya Gamboa,[1] Kelly Jara,[1] Howon Lee,[2,*] and Hatem E. Sabaawy[1,3,5,*]

SUMMARY

Glioblastoma is the most common and deadly primary brain malignancy. Despite advances in precision medicine oncology (PMO) allowing the identification of molecular vulnerabilities in glioblastoma, treatment options remain limited, and molecular assays guided by genomic and expression profiling to inform patient enrollment in life-saving trials are lacking. Here, we generate four-dimensional (4D) cell-culture arrays for rapid assessment of drug responses in glioblastoma patient-derived models. The arrays are 3D printed with thermo-responsive shape memory polymer (SMP). Upon heating, the SMP arrays self-transform in time from 3D cell-culture inserts into histological cassettes. We assess the utility of these arrays with glioblastoma cells, gliospheres, and patient derived organoid-like (PDO) models and demonstrate their use with glioblastoma PDOs for assessing drug sensitivity, on-target activity, and synergy in drug combinations. When including genomic and drug testing assays, this platform is poised to offer rapid functional drug assessments for future selection of therapies in PMO.

INTRODUCTION

Glioblastoma (GBM) is the most common and deadly primary brain malignancy (Siegel et al., 2020). The clinical suspicion of a brain tumor frequently follows a new onset of neurological deficits or seizures, with MRI being the imaging method of choice to detect brain tumors. However, a definite diagnosis of a GBM (World Health Organization grade IV brain tumor) can only be made histologically (Weller et al., 2015). Even when current therapies for GBM, including resection, irradiation, chemotherapy, and/or concurrent or adjuvant temozolomide (TMZ), are implemented shortly after diagnosis, tumors frequently recur, resulting in a median survival rate of patients with GBM averaging a dismal 15 months (Siegel et al., 2020). Extreme plasticity, the strong selective pressures occurring during early GBM development and with current therapies (Barthel et al., 2019), and intra- and inter-tumor heterogeneity in GBM, as revealed by single-cell RNA sequencing (scRNA-seq) studies (Neftel et al., 2019; Patel et al., 2014), impose the therapeutic failures. Moreover, the lack of patient-derived models of GBM that reflect these core elements of heterogeneity yet can be used to predict patient outcome; for instance predicting responses to therapy, resulted in high failure rates for many new drugs. In GBM, patient-derived models can be generated from bulk and/or GBM stem-like cells (GSCs). Although debated, the GSC phenotypic features (Gimple et al., 2019) and signaling pathways (Rajakulendran et al., 2019) could be employed to identify GBM molecular vulnerabilities in these models for examining targeted and personalized therapies. The Cancer Genome Atlas (TCGA) and other sequencing studies allowed the sub-classification of GBM into three molecular subtypes (Weller et al., 2015). However, scRNA-seq studies revealed that individual GBMs contain a spectrum of these subtypes (Patel et al., 2014), and are present in multiple cellular states within each tumor, with these states enriched by the genetic influence and/or the tumor microenvironment (TME) (Neftel et al., 2019).

Seminal studies established the ability of mammalian neural precursor cells, a presumed normal counterpart of GSCs, to respond to supplemented growth factors and to form either monolayer cultures of differentiated cells or free-floating spherical aggregates termed ‘‘neurospheres’’ (Reynolds and Weiss, 1992). Recent advances in three-dimensional (3D) culture allowed utilizing the remarkable self-organizing properties of embryonic stem cells (ESCs)/induced pluripotent stem cells (iPSCs) (Eiraku et al., 2008) to direct their neural developmental differentiation into human cerebral organoids, either in the presence

---

[1] Rutgers Cancer Institute of New Jersey, Rutgers University, New Brunswick, NJ 08901, USA

[2] Department of Mechanical and Aerospace Engineering, Rutgers University – New Brunswick, New Brunswick, NJ 08901, USA

[3] Departments of Medicine and Pathology and Laboratory Medicine, RBHS-Robert Wood Johnson Medical School, Rutgers University, New Brunswick, NJ 08901, USA

[4] These authors contributed equally

[5] Lead Contact

*Correspondence: howon.lee@rutgers.edu (H.L.), sabaawhe@cinj.rutgers.edu (H.E.S.)

https://doi.org/10.1016/j.isci.2020.101365

(Lancaster et al., 2013) or absence (Pasca et al., 2015) of extracellular matrix (ECM) scaffolds. Notably, cerebral organoids recapitulated key neural cell growth, organization, and differentiation (Lancaster et al., 2013), thus substantiating their use in tissue regeneration and tumor modeling. When derived from GBM patient biopsies and/or surgical specimens, patient-derived cells (PDCs), patient-derived spheres (PDSs, also called gliospheres, analogous to glial neurospheres), and organoid-like cultures could be established. The development of 3D patient-derived organoid-like (PDO) culture of human primary tumors allowed for the initiation and long-term propagation of these PDO cultures from biopsies and/or surgical resections of multiple cancers (Tuveson and Clevers, 2019), including the derivation of GBM-PDOs from patients with recurrent and treated GBM (Hubert et al., 2016). These models could also be utilized for generating patient-derived xenografts (PDXs) at heterotopic (frequently subcutaneous) sites and/or in the brain (patient-derived orthotopic xenografts or PDOXs) for *in vivo* studies. Nevertheless, the xenografts remain expensive to generate, time consuming, and may become clonally distinct from the originating GBMs (Patrizii et al., 2018). Remarkably, the powerful potential of PDOs in modeling treatment responses and predicting clinical outcome of patients enrolled in clinical trials has been noted (Vlachogiannis et al., 2018). Moreover, a recent case report demonstrated the potential of using PDOs for tailoring treatment in GBM (Loong et al., 2020). Yet, the generation of PDOs for drug testing is still laborious and lengthy, requiring multiple steps including establishing and transporting of PDCs and ECM between thousands of wells for dissociation; making PDOs; allowing cellular growth for weeks to months; performing drug treatment with multiple compounds; assessing cell viability and tumorigenic assays; cell fixation and antibody staining; histologic processing; and final immunohistochemical (IHC) validations. These lengthy and laborious steps with manual transfers between each step prohibit the wider use of these assays in translational studies and make them unsuitable for integration into clinical diagnostic tests and/or large-scale drug screening. Targeted therapies could be designed to counter GBM heterogeneity (Prados et al., 2015), yet drug testing in PDOs for targeted therapy is a tedious process taking weeks to months to complete (Vlachogiannis et al., 2018). In addition, whereas using hydrogel-based carriers allowed simultaneous histological processing of spheroids and organoids (Parker et al., 2020), samples in these carriers still required time-consuming manual transfers between culture and histology vessels, also subjecting the delicate spheroids and organoids to the possibility of undesired distortions during processing.

We have previously utilized PDSs from primary tumors to model tumor heterogeneity and develop therapies to target the self-renewing stem-like cells (Bansal et al., 2016; Bartucci et al., 2017). In parallel, advances both in 3D and 4D printing (with 4D printing referring to 3D printing with smart materials that are responsive to stimuli, programming them to evolve from one 3D shape to another) allowed generating devices, implants, and scaffolds for tissue engineering. Here, we first generated expandable/collapsible smart material arrays by 3D printing. Upon heating, these 4D printed arrays self-transformed from cell-culture inserts into histological cassettes. Self-transformation occurred inclusive of their GBM-PDO contents, which remained in the same configuration throughout the entire assay, therefore allowing for rapid programmable drug testing and assessing indicators of effective and synergistic GBM combination therapy.

RESULTS

Bioengineering of 4D Printed Cell-Culture Insert Arrays

As a first step toward streamlining pre-clinical studies of *ex vivo* models of GBM, we utilized 4D printing to fabricate the self-transformable cell-culture insert arrays. 4D printing refers to 3D prints with smart materials that change shape, properties, and/or functions in response to external stimuli, with the fourth dimension being time (Ge et al., 2016; Yang et al., 2019). The smart material utilized in this work was a shape memory polymer (SMP), and the high-precision 3D printing technique was projection micro-stereolithography (PμSL) (Zheng et al., 2012). Each cell-culture insert array consisted of interconnected wells and was capable of self-transforming, while maintaining the same layout, contents, and configurations, between the size of a standard 96-well plate and the size of a histology megacassette (3.6 times the overall dimensional change) (Figure 1 and Video S1). This process allowed completing the histological processing of the entire array in one sectioning step (see Transparent Methods). The SMPs could be fixed in a temporarily deformed shape (shape programming) and restored to the original shape (shape recovery) upon heating around glass-transition temperature (T_g) (Figures S1A and S1B). Each well of the cell-culture insert array consisted of a lower cell-culture compartment containing biological samples and four upper interconnecting helical bridges allowing self-transformation (Figures 1B and S1C). The self-transformable SMP cell-culture insert arrays were mounted on 96- or 6-well plates. The arrays were utilized for assessing the establishment of GBM PDCs in

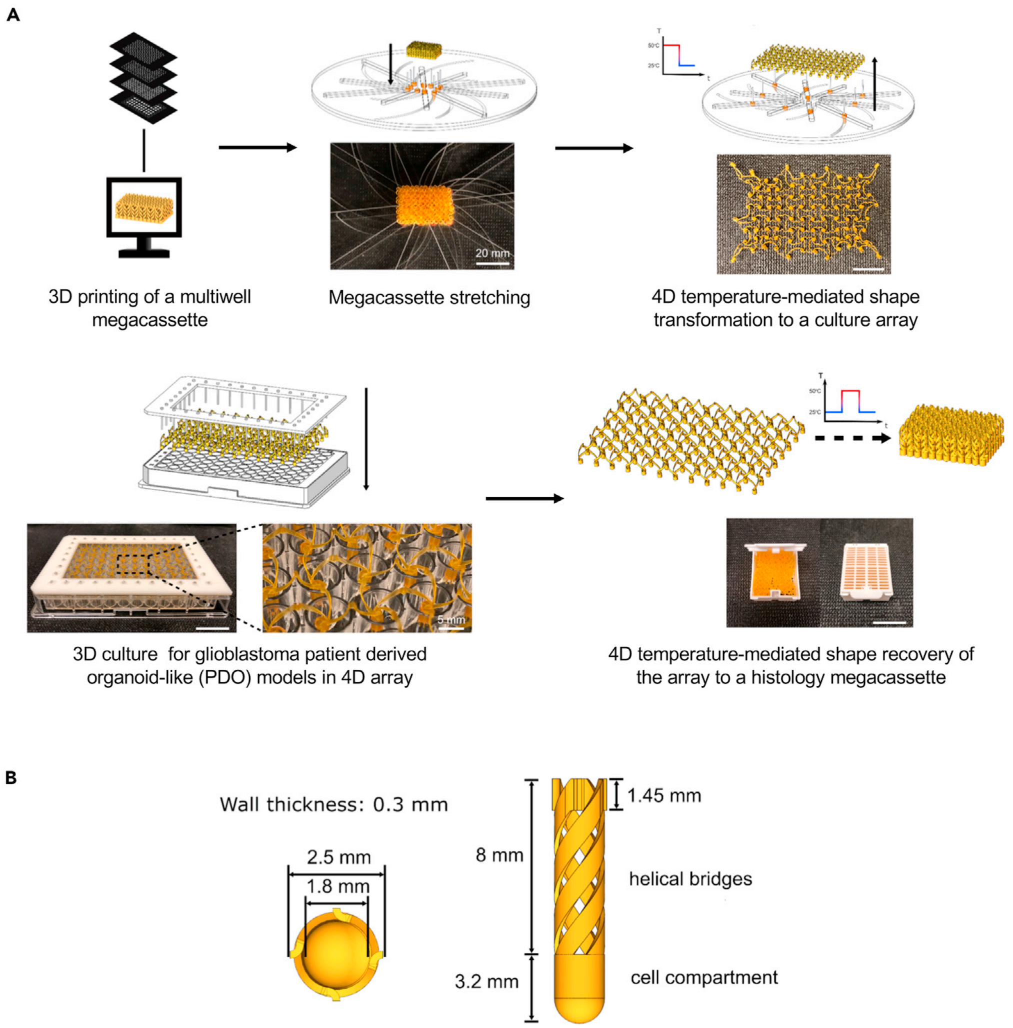

Figure 1. Diagrams Representing Step-by-Step Operating Procedures of the 4D Cell-Culture Insert Array Shape Transformation

(A) At room temperature (RT), an insert in the cassette configuration was first mounted on a custom-built stretcher. The stretcher has eight rails that can simultaneously move all carriages sitting in rails between the dimension of a cassette and the dimension of a 96-well plate. The insert was stretched to a 96-well plate configuration by simply rotating the top and bottom plates against each other at RT. All helical bridges are unwound during the rotation of the stretcher. After rotation, both the insert and the stretcher were placed in an oven at 50°C for 10 min and then cooled down to RT to program the stretched shape. The insert array was then removed from the stretcher with the temporarily programmed shape. Cell-culture insert arrays were then mounted onto a fixture that has a perfect matching between edge units of the insert and a 96-well plate. The fixture with the insert was then placed on a 96-well plate for cell seeding. Cells, culture media, and treatment compounds were injected into insert wells using micropipettes (see Transparent Methods). After 3D cell culture, the insert was removed from the fixture and heated to 50°C to induce a shape recovery to the cassette configuration while maintaining the registry of the cultured cells. In the cassette configuration, the insert was ready for histological processing to obtain the histology of the entire cell-culture array.

(B) The diagram displays top and side views and the corresponding dimensions of an individual well component of the 4D printed cell-culture insert array. See also Figures S1 and S4 and Video S1 for demonstrations of the thermomechanical properties of the 4D printed cell-culture insert array and Figures S5–S7 for data determining the biocompatibility of these cell-culture arrays.

3D PDSs and GBM-PDO cultures for 1 or 2 weeks or up to 12 weeks, respectively, after which cells were fixed and the entire cell-culture array self-transformed back to the size of a histology megacassette. Shape transformation was followed by microtome sectioning, staining, and imaging within the same platform, thus remarkably expediting the processing of these multiple histological assays. We first compared the growth

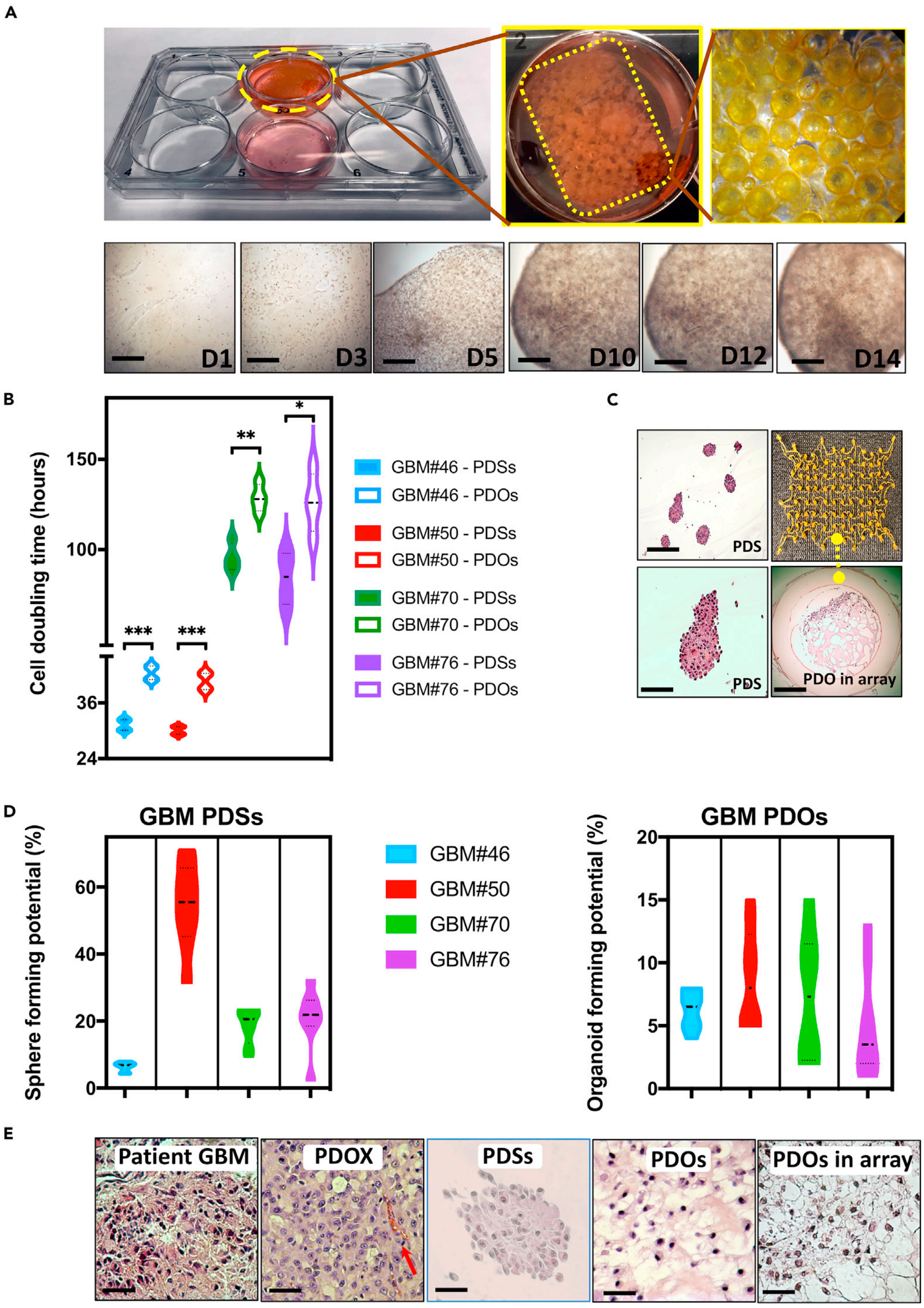

Figure 2. Utilization of SMP Cell-Culture Insert Arrays for Histological Processing of GBM-PDOs

(A) Diagram displaying the cell-culture array when used in 6-well plates, and bright-field images of 14-day 3D PDO culture. Complexity of the organoid structures increased with time.

(B) Average cell doubling times during the first week of PDS and PDO culture from four patients with GBM.

(C) After 6–14 days of 3D PDS and/or PDO culture alone or in the array, PDSs and PDOs were fixed and stained with H&E. Images demonstrate a group of representative PDSs derived from GBM#50, with the lower image being a 4× magnification of a PDS in the top image. The lower right image demonstrates the phenotypes of PDOs from GBM#46 when cultured in the array.

Figure 2. *Continued*

(D) Sphere- and organoid-forming potentials were assessed using extreme limiting dilution analysis software at http://bioinf.wehi.edu.au/software/elda/. The frequencies based on log-fraction plot of the dilution model, log-active cell fractions, and 95% confidence interval are indicated from four GBM-PDSs and GBM-PDOs.

(E) Histological H&E analysis of original tissue (GBM#46), PDOXs generated from the same patient cells, PDSs, PDOs, and PDOs in the cell-culture insert array collected and fixed after 14 days of culture. Note that the cell density is different in patient and PDOX sections because the cell density depends on the number of engrafted or plated cells. See additional features of these PDSs and PDOs in Figure S2.

Comparison of doubling times and clonogenic potentials between PDSs versus PDOs in (B and D) are represented as mean ± SD of four replicates and were determined by two-way ANOVA with Bonferroni post-hoc test (***$p < 0.001$, **$p < 0.01$, *$p < 0.05$). Scale bars, 100 μm in (A, C, and E).

conditions of GBM cells in our cell-culture arrays with the existing approaches using PDCs and GBM cells in 2D surface-coated adherence culture, 3D PDSs, and GBM-PDO cultures.

GBM-PDO Cultures Model Key GBM Features

Primary GBM were obtained from GBM patients undergoing craniotomy resection at Robert Wood Johnson University Hospital under an Institutional Review Board-approved protocol. Live cells were maintained in conditions to generate and maintain GBM PDSs (Mehta et al., 2015) or were used to generate organoid-like GBM-PDOs in conditions developed in our laboratory (see Transparent Methods), which were modified from those used to generate cerebral organoids (Lancaster et al., 2013) and GBM-PDOs (Hubert et al., 2016). Single cells were seeded at clonal densities in ultra-low attachment plates with culture inserts in serum-free growth factor-supplemented conditions for PDSs or in ECM droplets within inserts for GBM-PDOs (Figure 2A). To compare GBM-PDCs, GBM-PDSs, and GBM-PDOs in our system, we assessed if they resembled their corresponding originating tumors. We performed histological analyses and assessed variability in size, nuclear morphology, and cytologic features. Each PDS and PDO was independently confirmed by a neuropathologist to show key histological features of high-grade gliomas such as solid growth and diffuse invasive appearance using H&E staining. Although PDS cells multiplied significantly faster in the first 3–5 days when compared with PDO cells (Figures 2B and S2A), PDSs were smaller than PDOs at 2 weeks (PDSs: 100–300 μm, PDOs: 400–600 μm) (Figure S2B). GBM-PDOs grown in the 4D printed arrays were also larger than PDSs (Figure 2C). PDSs were still smaller than GBM-PDOs after 12 weeks of culture, where GBM-PDOs could be expanded to sizes reaching 2–3.5 mm (Figures S2B and S2C).

Quantitative analysis showed that PDSs had widely varying clonogenic sphere-forming potentials (Figure 2D). In contrast, clonogenic organoid-forming potential among GBM-PDOs were more uniform (Figure 2D). When compared morphologically with PDSs, GBM-PDOs showed notable pleomorphism in the central core and outside rim regions with significant variability in cell size, nuclear morphology, and cytologic features (Figure 2C). When examined histologically, GBM-PDOs showed histological features in H&E resembling the originating GBM patient tissue (Figure 2E). They also generated similar histological features when xenografted into the adult immune-deficient NSG mouse brain (Figure 2E), following procedures we described previously (Patrizii et al., 2018) (see Transparent Methods).

To characterize the cellular subset distribution within PDSs and GBM-PDOs from all four patient tumors, we examined neurodevelopmental markers associated with highly undifferentiated grade IV glioma and markers of self-renewal and differentiation by immunocytological assays. It was previously shown that the neurosphere assay enriches for neural stem cells (NSCs) and also likely GSCs, and when basic fibroblast growth factor (bFGF) and epidermal growth factor (EGF) are removed from media or PDCs are cultured in the presence of serum and/or on polyornithine-coated surfaces, GBM cells undergo GSC loss (Mehta et al., 2015). Unlike PDSs that were enriched in NESTIN-expressing cells in the outer rim (Figure 3A), and PDCs that downregulated NESTIN but showed relatively more differentiation expression profiles toward mature astrocytic glial fibrillary acidic protein (GFAP)- and neuronal tubulin-beta-III (TUJ1)-expressing cells, we observed robust heterogeneity in size, cell identity, and morphology in GBM-PDOs between 2 and 12 weeks of culture (Figures 3B and S2). NESTIN expression was notably slightly denser near the outer rim of GBM-PDOs, perhaps due to the proximity to the stimulatory growth factors (EGF, bFGF). Yet, unlike PDSs, NESTIN was still present in cells within the GBM-PDO inner core. There was less dense overall staining in the GBM-PDO core, with the GBM-PDO centers containing multiple cellular areas in between the ECM (Figures 3B, 2E, and 4). Remarkably, 3D cultured genotypically matched GBM-PDOs remained heterogeneous when cultured in the 4D printed insert arrays for weeks and were capable of interconnecting

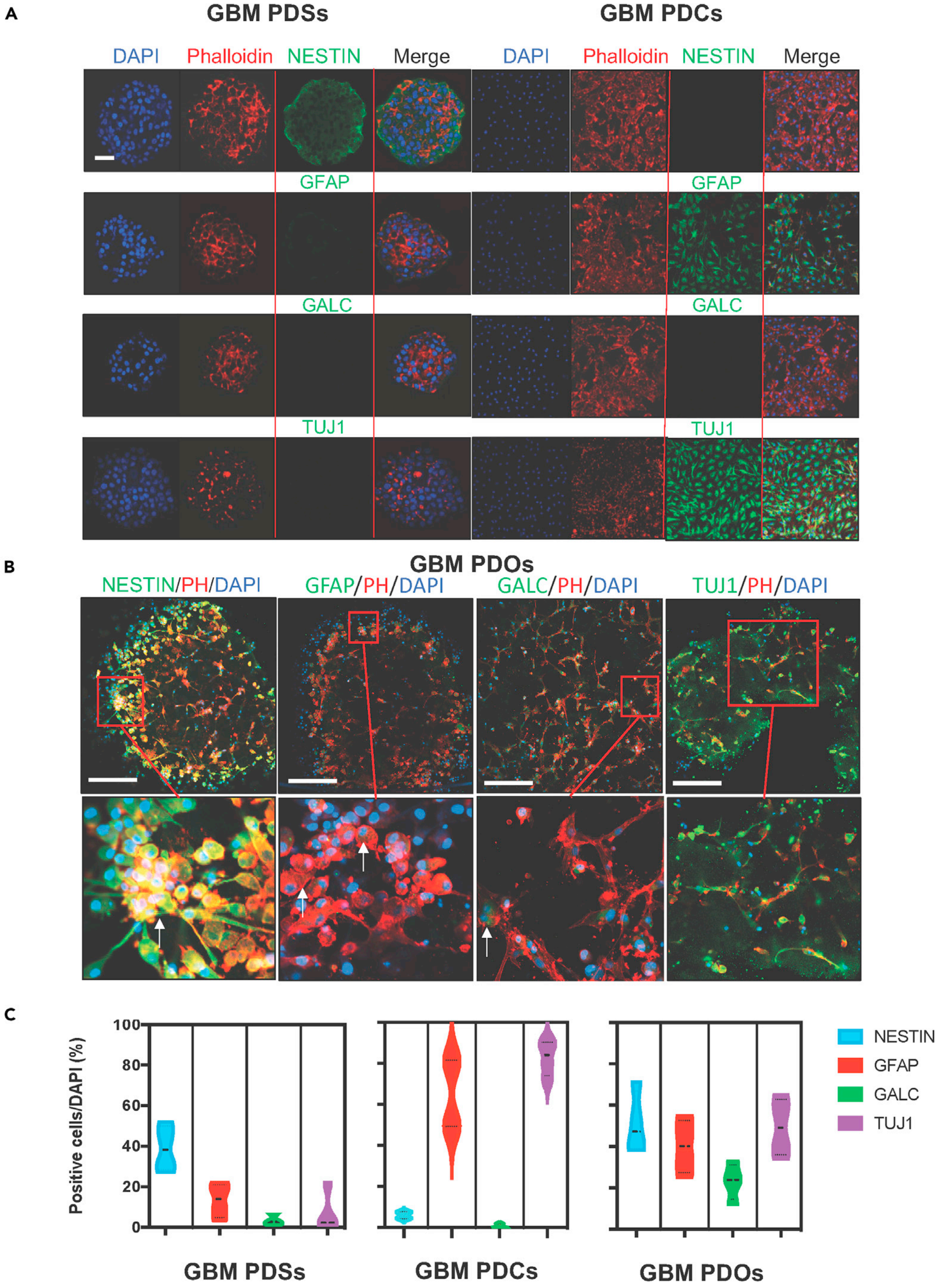

Figure 3. Comparing Cellular Components of Patient-Derived Models of GBM-PDCs, GBM-PDSs, and GBM-PDOs

(A) Immunofluorescence (IF) for NESTIN, which is used as a neuroepithelial progenitor marker, and glial fibrillary acidic protein (GFAP), galactosidase C (GALC), and tubulin-beta-III (TUJ1) (neuroepithelial differentiation markers). GFAP is used as a marker of CNS mature astrocytes and ependymal cells. GALC is a marker for early-stage oligodendroglia. TUJ1 is a neuron-specific early marker of signal commitment in primitive neuroepithelium. DAPI is used to label the nuclei, whereas phalloidin is used to mark the cell architectures within the PDCs, PDSs, and PDOs. Note that PDSs formed after GBM 3D culture for 1 week are enriched with NESTIN expression but not differentiation markers, but when the formed spheres were then cultured on polyornithine plates for an additional 10 days, GBM cells (PDCs) differentiated with partial expression of some differentiation markers detected.

Figure 3. *Continued*

(B) IF assays of GBM PDOs formed after 14 days of 3D PDO culture. PDOs readily express various progenitor (NESTIN in green) and/or differentiated neural markers (GFAP, GALC, or TUJ1 in green), representing GBM phenotypic cell heterogeneity. Images represent an overlay of green (NESTIN, GFAP, GALC, or TUJ1), red (phalloidin [ph]), and blue (DAPI [D] for nuclei) confocal images. Scale bars in (A) and (B) are 100 μm.

(C) Violin plot quantitation of phenotypic PDO expression profiles represented as mean ± SD from four representative GBMs in six independent experiments.

(mimicking brain cells) and showing multiple cell phenotypes (Figures 3B and 4). Quantitative analysis showed that although PDSs are enriched in NESTIN-expressing neuroepithelial progenitors, they featured less GFAP-, galactosidase C (GALC)-, and TUJ1-expressing cell types (Figure 3C). These cellular subtype distributions were essentially reversed in PDCs cultured on polyornithine plates (or when bFGF and EGF were replaced with serum). PDCs downregulated NESTIN and featured GFAP- and TUJ1-expressing cells, but GALC was consistently less clearly detectable (Figure 3A). Therefore, PDSs and PDCs demonstrated distinct self-renewal and differentiation profile enrichment. On the other hand, GBM-PDOs demonstrated balanced NESTIN- GFAP-, GALC-, and TUJ1-expressing cell phenotypes (Figures 3B and 3C). NESTIN-expressing cells in the outer rim coexpressed other GSC markers like the orphan nuclear receptor tailless (TLX) (Figure 4A) and the iPSC and self-renewal protein SOX2, with TLX and SOX2 expressions being widely detected in PDSs, both at the outer and inner cores, albeit at lower levels in the inner core (Figures 4A and 4B).

Transcriptional heterogeneity in GBM may reflect differences in chromatin compaction modified by the epigenetic polycomb repressive complex-1 (PRC1), which comprises the self-renewal protein BMI1; also GBM with mesenchymal transcriptional profiles showed enrichment of a BMI1 activation signature (Jin et al., 2017). Moreover, both BMI1 expression and activation signatures were associated with poor patient prognosis (Jin et al., 2017). Therefore, we compared BMI1 expression in PDSs and GBM-PDOs (Figures 4C and 4D) and correlated their levels to BMI1 levels in the originating GBMs (Figures 4C–4E and S3A). Similar to SOX2 and TLX expression profiles, BMI1 expression was enriched in PDSs when compared with the corresponding originating GBM from three patients, whereas BMI1 levels in GBM-PDOs were overall in line with those in the originating GBMs and their derived PDOX (Figure 4E). These data suggest that PDS profiles limit the ability to study heterogeneous GBM cell populations simultaneously, whereas the profiles of GBM-PDOs more relatively resemble GBM cellular subtype heterogeneity. We therefore utilized these GBM-PDOs to validate the use of the SMP cell-culture array in drug testing.

Biocompatibility of the Cell-Culture Insert Arrays

To examine the biocompatibility of the cell-culture arrays for generating GBM-PDSs and GBM-PDOs for histological processing and imaging, we first established optimum seeding densities for 3D cultures (see Transparent Methods) to test the culture inserts. We quantified PDS and PDO number, viability, and differentiation potential upon shape recovery of the inserts at 50°C. We were able to reduce the cell fixation time from an overnight fixation or fixation for several hours to fixation for 1 h. These data are in support of SMP compatibility with paraformaldehyde fixation, while maintaining cellular integrity either in individual inserts or complete arrays in the 12-step histological assays (Figure S4).

We examined the effects of SMP components on cell viability both in U87MG and primary GBM 3D cultures. U87MG cells and primary GBM#50 PDSs or PDOs grown with the arrays in the first prototype array initially failed to proliferate (Figure S5), even though the controls not included in the arrays, particularly GBM#50, exhibited normal growth, larger spheres, and diversified organoid-like growth with multicellular connection after 1 or 2 weeks (Figure S5). To assess any potential toxicity, we measured media levels in prolonged cultures and determined that the arrays were not absorbing media, thus limiting growth factor availability. In addition, 2-week culture media were slightly more alkaline compared with controls, suggesting that the arrays could be leaching a low-level chemical that may interfere with long-term GBM-PDO cultures. SMP components, including PEGDA 250, BPADMA, PI, and PA were each examined using the intracellular ATP cell viability assays. Only PEGDA250, when used at a three-log higher concentration of its median dose (1,000-fold in excess of EC_{50}, which was 7.2 μM) significantly impacted cell viability (Figure S6), suggesting that low PEGDA 250 levels may be leaching from the inserts in prolonged GBM-PDO cultures. Preincubation of the insert array after 3D printing in culture media, PBS, 10% BSA, or β-mercaptoethanol (at 10 or 50 μM) did not reverse the cell loss phenotype, but pre-soaking in 100%

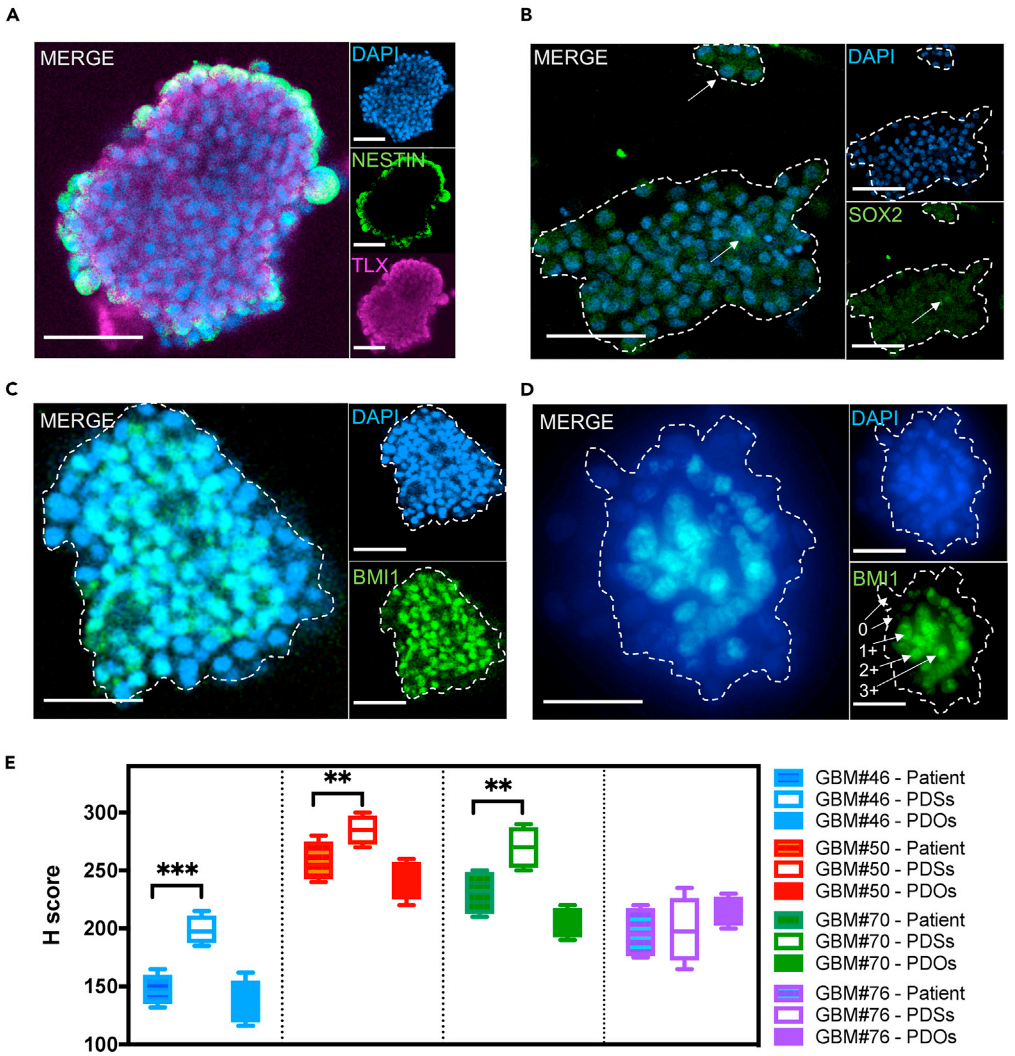

Figure 4. Phenotypic Cellular Heterogeneity in GBM-PDOs

(A) IF mosaic imaging of NESTIN (green) and TLX (purple) proteins in GBM#76 PDSs.

(B) SOX2 (green) protein expression in nuclei (arrows) of GBM#76 PDSs.

(C and D) BMI1 IF from GBM#46 with PDSs (C) and PDOs (D). Images are representatives from three independent experiments. Scoring of IF level (0–3+) is demonstrated in (D) next to each corresponding representative cell. The PDS and PDO magnified regions of the mosaic span are indicated by dashed outlines. Scale bars in (A–D) are 100 μm.

(E) Images were quantified for the amount of BMI1 positive staining, as well as for intensity of the staining. For quantitative analyses of IF and IHC from patient tissues, H scores were calculated as (% at 0) × 0 + (% at 1+) × 1 + (% at 2+) × 2 + (% at 3+) × 3 = Range 0–300 based on analyses of at least 10 fields per slide averaged by two qualified examiners. Representative images and analyses of BMI1 expression in GBM tissues and PDOXs can be seen in Figure S3A. Comparison of H scores between patient tissues versus PDSs and PDOs are represented as mean ± SD of counts from two independent observers, and comparisons were determined by two-way ANOVA with Bonferroni post-hoc test (***$p < 0.001$, **$p < 0.01$).

acetone followed by PBS and ethanol washes did (Figure S7). Based on these data, we established the conditions for use of 4D printed SMP arrays for GBM-PDO generation and drug sensitivity assays.

Identifying GBM Molecular Subtypes for Examining Targeted Therapy

GBM patient tissues are routinely subjected to targeted exome sequencing (Glioseq) at our hospital. Glioseq analyzes 30 genes for single-nucleotide variants or indels, 24 genes for copy number variations (CNVs), and 14 types of structural alterations in BRAF, EGFR, and FGFR3 genes in a single workflow

A

Patient	Age	Sex	Diagnosis	Ki67 %	PDO#s	PDO NGS findings (Mutational rate: %)
#46	46	M	1^{ry} GBM	<10%	++	- TERT mut (58.5) - NF1 del (33.9) - PTEN splice variant (99.9) - ATRX mut (99.7) - CDKN2A copy number LOSS
#50	75	F	1^{ry} GBM	40%	+++	- TERT mut (57.8) - NF1 del (31.6) - PTEN splice variant (99.9) - ATRX mut (99.6) - CDKN2A copy number LOSS
#70	39	M	1^{ry} GBM	<5%	++	- TERT mut (53) - NF1 mut (31.4) - PTEN splice variant (99.8) - ATRX mut (99.8) - CDKN2A copy number LOSS
#76	77	F	1^{ry} GBM	8%	++	- TERT mut (53.8) - NF1 mut (30.1) - PTEN splice variant (100) - ATRX mut (99.7) - CDKN2A copy number LOSS

B

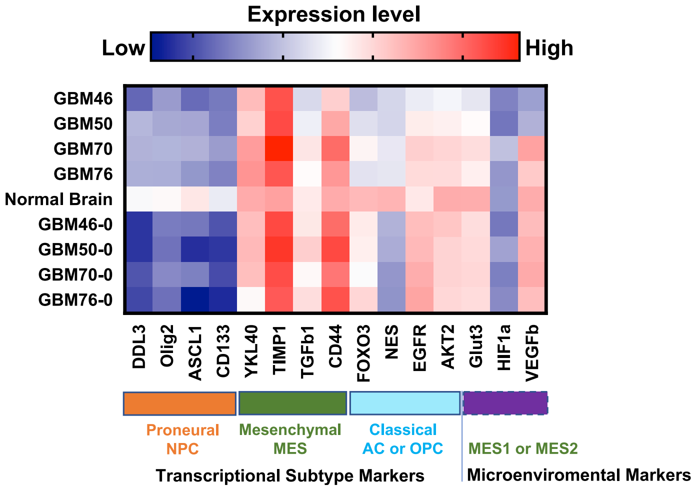

Figure 5. Targeted Exome Sequencing and Molecular Subtype Profiling of GBMs

(A) Summary of GBM patient profiles, molecular features, Glioseq profiles, and outcome based on targeted exome sequencing of originating tissues and corresponding GBM-PDOs.

(B) Heatmap of the molecular subtype and microenviromental marker expressions in four GBM samples displayed against a pool of five nonmalignant normal human brain samples, and the corresponding originating resected GBMs (labeled with a zero). *Z* scores in the heatmap are represented as mean expression levels and were calculated from qPCR ΔCt values from three independent experiments. See also Figures S3B and S3C for assessments of TP53 and CDKN2a expression in these GBMs.

(Nikiforova et al., 2016). We analyzed Glioseq data to guide the selection of potential targeted therapies (Figure 5A). Glioseq findings revealed that GBM-PDOs from GBM#46, GBM#50, GBM#70, and GBM#76 had mutations in TERT, NF1 deletions, PTEN splice variants, ATRX mutations, and CDKN2A copy number loss. Further genomic and molecular analyses revealed that cells from these GBMs had WT exon 5 p53 without detectable hotspot mutations, but they showed no detectable expression of CDKN2a (Figure S3B), suggesting that CDKN2a copy number losses are homozygous in these cells, a common GBM feature (Weller et al., 2015).

Recent scRNA-seq-based models support that GBM cells remain heterogeneous, exhibit plasticity, and exist in four main cellular neurodevelopmental states: mesenchymal (MES), astrocytic, oligodendroglial precursor cell, and proneuronal progenitor cell states (Neftel et al., 2019). We performed GBM subtype gene signatures and gene expression profiling using a subset of markers based on TCGA database and signatures associated with tumor histology, grade, and defining molecular features (Jin et al., 2017).

GBM46, GBM50, GBM70, and GBM76 displayed MES transcriptional gene expression profiles (Figure 5B). The frequency of cells in each GBM cellular state is influenced by CDK4, EGFR, and PDGFRA CNVs, as well as NF1 mutations (Neftel et al., 2019). Glioseq analyses revealed no CNVs in CDK4, EGFR, or PDGFR, but identified NF1 deletions or mutations in all four GBMs. As high expression of mesenchymal-related genes together with either high or low hypoxia-response genes defines either mesenchymal-like hypoxia-independent (MES1) or mesenchymal-like hypoxia-dependent (MES2) signatures, respectively (Neftel et al., 2019), we surmized that GBM46 and GBM50 PDOs have relatively matching MES1 signatures and were chosen for subsequent drug sensitivity assays.

Evaluation of Targeted and Combination Therapy

For GBM-PDO drug sensitivity assays, single cells were seeded at clonal densities in ultra-low attachment plates with culture inserts in serum-free growth factor supplemented conditions for PDS formation and within ECM droplets in inserts for GBM-PDO formation. After 2 weeks, clonal GBM-PDOs were treated for 72 h with either the standard chemotherapy TMZ and/or molecularly targeted agents, targeting mTOR, PI3K, or DNA damage response (DDR) among others. Following treatments, the entire 4D printed cell-culture arrays self-transformed to their original programmable cassette size upon heating for 20 min, for direct histological and IHC processing on the same day, while maintaining the starting tissue and array orientation and configuration. Interestingly, drugs tested had varying effects on different GBM-PDOs. TMZ was effective at reducing viability in GBM#46 more than GBM#50, whereas BEZ-235, a PI3K/mTOR dual inhibitor, was more effective in GBM#50, illuminating inter-tumor heterogeneity between GBM patient samples even with relatively similar molecular subtypes (Figure 6A). To test our hypothesis that combining compounds targeting GBM cell survival signaling in GBM cells with PTEN mutations (by targeting PI3K/mTOR signaling), NF1 and/or ATRX mutations (by using niraparib), and DDR (also by using niraparib), we assessed these combinations against TMZ in GBM-PDOs (Figure 6). Targeted therapies resulted in significantly higher antitumor activities relative to TMZ in GBM#50. To assess the synergy of two compounds in combination therapy, a Bliss independence model (Ianevski et al., 2017) for combination matrix surface evaluation was utilized for the combination of TMZ plus BEZ235 or niraparib plus BEZ235 treatment of GBM-PDOs. These studies revealed that whereas BEZ235 may protect from TMZ toxicities (Figure 6B), BEZ235 and niraparib could act synergistically (Figure 6C). We also assessed apoptosis induction, GBM cell migration, and ECM invasion using live cell imaging and fluorescent cell monitoring of treated GBM-PDOs by measuring the levels of activated caspase 3 (Figures 7A and 7B) and EGFP fluorescent migrating or invading GBM-PDO cells (Figures 7C and 7D). The results indicated that combination therapy increased apoptosis in GBM#46 PDOs that were relatively less sensitive to TMZ (Figures 7B–7D) and could significantly reduce migration and invasion of GBM-PDO cells compared with TMZ (Figures 7C and 7D), complementing the cell proliferation assays. Moreover, we detected on-target activities of these therapies by immunofluorescence against the GBM hallmark GFAP, GSC marker BMI1, and PI3K/mTOR marker pS6 (Figures 7E and 7F), providing rationale for further validating these combination therapies. In total, these data demonstrate that our developed system could be used for rapid histological processing and drug sensitivity testing in GBM-PDOs.

DISCUSSION

We developed the first example of 4D printed programmable cell-culture arrays using a thermo-responsive SMP for cancer drug testing. We used these arrays for histological assessment and drug testing of targeted and combination therapies in single cell-derived GBM-PDOs. 4D printing, which is defined as 3D printing with smart materials that are responsive to stimuli, offers the facile advantages of free-form fabrication and microfluidic approaches for drug discovery (Lee and Cho, 2016). We demonstrated the printability and biocompatibility of the SMP material in 4D printing. We utilized a high-precision additive manufacturing technique, PμSL (Zheng et al., 2012), for 3D printing to fabricate the SMP constructs that self-transform between 3D cell-culture insert arrays and 3D histology cassettes. Our 4D printing approach addresses the current limitations in processing 3D models by allowing for the scaling of screening capacity and simultaneous processing of organoid models for higher-throughput analysis, as recently done with cerebral organoids (Parker et al., 2020). Added advantages of our 4D printing approach is the programmable self-transformation between 3D arrays and 3D histological cassettes, therefore eliminating the time-consuming manual transfers, with their associated possibility of distortion or damage of delicate PDS and PDO biological samples. Moreover, the biological samples remain in the same configuration within the cell-culture

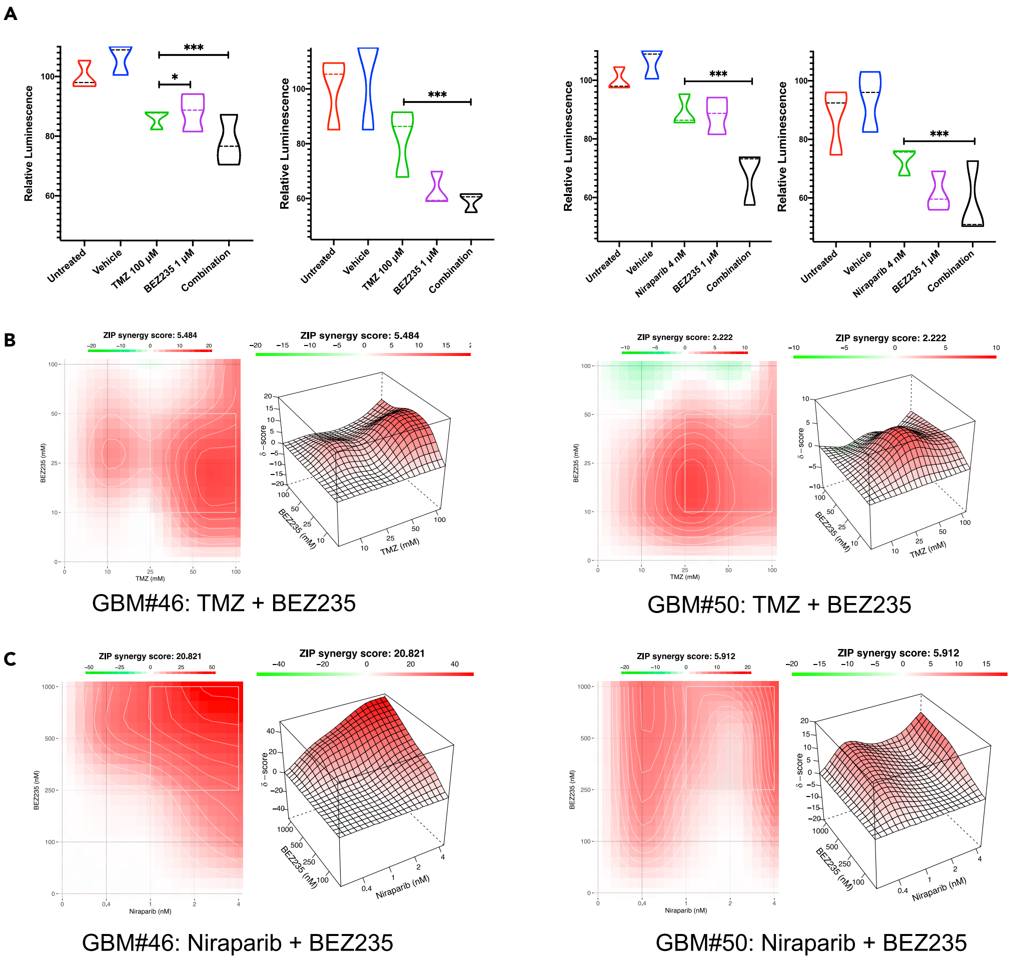

GBM#46: TMZ + BEZ235

GBM#50: TMZ + BEZ235

GBM#46: Niraparib + BEZ235

GBM#50: Niraparib + BEZ235

Figure 6. Assessing Targeted and Combination Therapy in GBM-PDOs

(A) Treatment effects on GBM cell viability demonstrated in violin plots by measuring intracellular ATP levels of treated cells compared with untreated cells from the same patient GBM-PDOs. Dosage selection for each GBM-PDO was determined based on growth-inhibitory concentrations. Note the better antitumor effects for targeted therapies and combination (Comb.) therapies at equal concentration (1X of [growth inhibitory conc. at 50%] GI_{50} conc. for each drug), when compared with standard TMZ treatment. Data represent treatment of six independent experiments in GBM-PDOs from GBM#46 (left panels) and GBM#50 (right panels). Results are mean ± SD of eight replicates, and significance was determined using two-way ANOVA (***$p < 0.001$).

(B) Isobologram for calculation and visualization of synergy scores from reduced GBM cell proliferation measured by ATP levels and synergistic response of the Bliss score surface assessed using the combination of TMZ plus BEZ235.

(C) Bliss score surface observed using the combination of niraparib plus BEZ235. Bliss plots were generated using the SynergyFinder application (Ianevski et al., 2017).

compartment of our arrays during the entire process, therefore expediting this process and increasing compatibility with high-throughput assays.

Other advanced 3D printing approaches used to generate GBM models included the bioprinting of GBM-on-a-chip (Yi et al., 2019) or hydrogel meshes laden with polymeric particles (Mirani et al., 2019). Overall, these approaches including organ-on-a-chip technologies are being explored to advance organoid studies for the development and application of organoid-on-a-chip technologies. The transformable SMP cell-culture insert arrays allowed the rapid generation of GBM-PDOs for drug testing and assessing synergy between targeted therapies in a single assay.

We utilized GBM tumors from treatment-naive patients and cultured the cells in 3D serum-free conditions to maintain GBM-PDSs (Mehta et al., 2015), and/or generated organoid-like GBM-PDOs (Hubert

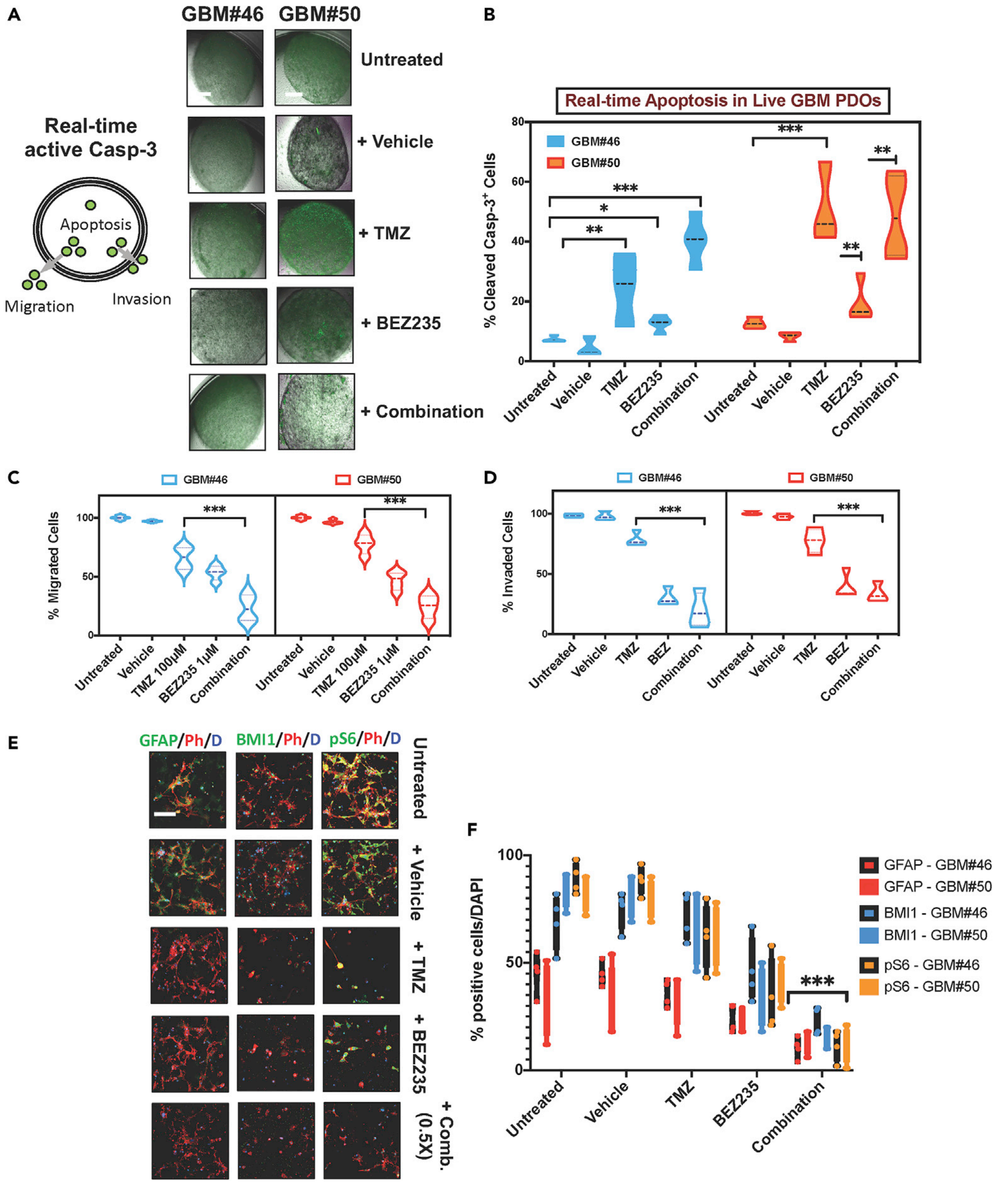

Figure 7. Detecting Antitumor Activities of Targeted Therapy and On-Target Activity in Live GBM-PDOs

(A) Left, model depicting detection of activated caspase-3 (Casp-3) activity by DEVD-NucView488 and live GBM-PDO cell population-averaged apoptosis, migration, and invasion assays. Right, the diagram displays the PDO-activated caspase-3 assay. GFP-positive cells within the organoids indicate apoptotic cells. GBM cells that invade the semisolid extracellular Matrigel represent invading cells, whereas cells that migrate outside of the organoid represent migrated cells.

(B) Comparison of cell viability and activated caspase-3 between untreated, DMSO, TMZ, and targeted therapy groups was determined by two-way ANOVA with Bonferroni post-hoc test. Graph indicates significance versus TMZ with $^{*}p < 0.05$, $^{**}p < 0.01$, $^{***}p < 0.001$. Violin plot on the top right represents real-time measurement of apoptotic cells in GBM-PDOs from GBM#46 and GBM#50 as untreated, DMSO-treated, or in response to treatment with TMZ, BEZ (targeting mTOR/PI3K), and combination therapy.

(C) GBM PDO cell migration captured by phase contrast using the IncuCyte HD system. Frames were captured at 4-h intervals from time 0 to 72 h from two separate regions/well using a 10× objective. Image processing involved fluorescent color channel separation, data resizing, illumination adjustment, threshold setting, and data extraction for either GBM#46 PDOs or GBM50 PDOs. Representative results of three separate experiments are shown for GBM#46 and GBM#50 as percentages of cell migration relative to 72-h values of untreated PDO cells.

Figure 7. *Continued*

(D) GBM-PDO cell invasion images were captured similarly with the IncuCyte HD system and shown as percentage of migrated cells relative to 72-h values of untreated GBM-PDO cells. Values determined by two-way ANOVA with Bonferroni post-hoc test (***$p < 0.001$).

(E and F) (E) Three key on-target activity markers were detected in PDOs in response to drug treatments: GFAP (hallmark of GBM), BMI1 (GSCs), and phospho-S6 (PI3K/mTOR activity). Representative confocal images were taken after the indicated treatments in fixed PDOs and represent overlay of green (GFAP on the right, BMI1 in center, and pS6 on the left), red (phalloidin), and blue (DAPI for nuclei). (F) Data represent quantitation of marker expression upon treatment from six independent experiments utilizing GBM-PDOs, GBM#46, and GBM#50. Results are mean ± SD of eight fields of at least 1,000 cells. Comparison of marker expression between combined versus single therapy groups was determined by two-way ANOVA with Bonferroni post-hoc test (***$p < 0.001$). Scale bars, 100 μm in (A and C).

et al., 2016; Lancaster et al., 2013). We demonstrated that GBM-PDOs contain highly heterogeneous cellular subtype populations, recapitulating the key expression profiles and tumor cell phenotypes in patients with GBM. The potential of PDO models to recapitulate aspects of GBM biology and heterogeneity is valuable. PDXs in mice, although may be useful in predicting clinical responses (Rokita et al., 2019), remain expensive, are variable in take rates, are time consuming to generate, and may become clonally distinct from originating GBMs (Patrizii et al., 2018). In addition, the phenotypes of GSCs remain debated, with single markers being variable in their expression among different tumors and PDS or PDX conditions. The use of combinations of stem cell markers in these models, although preferable, still might present differently than in human GBM. Cerebral organoids derived from human ESCs/iPSCs were genetically engineered to develop tumors with distinct oncogenic and tumor suppressor alterations and originating cellular identities (Bian et al., 2018), or by inducing mesenchymal GBM-like organoids with $\mathrm{HRas}^{\mathrm{G12V}}$ activation and p53 disruption (Ogawa et al., 2018). GBM heterogeneity was also modeled by co-culture of patient-derived GSCs with cerebral organoids, where GSCs proliferated over time and integrated into the normal cerebral organoids (Linkous et al., 2019). Most recently, propagating GBM tissues into smaller pieces has been shown to maintain the genetic and molecular signatures of GBM in 3D culture models, when tested within the first 2 weeks (Jacob et al., 2020). We utilized GBM-PDOs propagated for 2 weeks for drug testing, as we demonstrated that they contain heterogeneous cellular subtype populations, recapitulating the expression profiles and tumor cell phenotypes in patients with GBM. Although we could identify potential contributions of the TME cellular components to the expression profiles of our organoid-like GBM-PDOs, a comprehensive assessment of these TME cellular components will be performed in future studies to conclude their phenotypic nature while considering GBM plasticity (Neftel et al., 2019). Unlike the largely epithelial-only PDO models developed, a platform for generating PDOs using an air-liquid interface (ALI) method allowed retaining the native myoepithelial and immune cells, thereby preserving the immune contexture and recapitulating key elements of TME diversity (Neal et al., 2018). These ALI PDOs could be used to assess responses to immune checkpoint inhibition (Neal et al., 2018), therefore advancing PDO modeling toward more complete representation of the tumor and TME cellular components. Our cell-culture arrays may be utilized with many of these models and may be used to validate the potential of pharmacological, targeted, and immunotherapy for GBM.

Despite extensive efforts in defining morphological characteristics, complex molecular signatures, biomarkers, and imaging parameters of GBM that could provide biological tools for selecting GBM therapies, most treatment decisions for patients with GBM are still based on age and performance criteria. Moreover, targeted therapy agents have shown minimal efficacy in molecularly informed clinical trials, largely because of the inadequate consideration of the multitude of biological differences existing between individual patients with GBM. Integrated sequencing strategies provided a broader understanding of the genomic landscape and selective pressure occurring both during early GBM development and with current therapies (Barthel et al., 2019). On the other hand, single-cell sequencing analyses revealed multiple patterns of intratumor heterogeneity and inherent molecular complexity of GBM (Neftel et al., 2019; Patel et al., 2014). Clearly, it will be necessary to cotarget multiple alterations in GBM using combination therapy (Sabaawy, 2013). Indeed, PMO studies provided recent evidence that personalized treatment with combination of customized agents could improve outcomes in patients with refractory malignancies (Rodon et al., 2019; Sicklick et al., 2019). To rationally select agents in combination with standard-of-care TMZ-based chemoradiotherapy for GBM, other US Food and drug Administration-approved therapies targeting pathways that contribute to GBM heterogeneity should be considered. These include drugs (1) with direct targets (e.g., EGFR, PDGFRA, BRAF) that are subsets of significantly mutated genes identified in GBM TCGA and/or with integrated analyses (Barthel et al., 2019), (2) that map to a pathway that is targeted by an approved drug or investigational agents (e.g., PTEN, PIK3CA, NF1, ATRX, and other DDR targets), or (3) that influence cellular plasticity or subclonal dynamics (Vinci et al., 2018). We utilized 4D printing of SMP arrays that were used to derive single-cell clonal GBM-PDOs to assess the effects of treatment with TMZ and/or combinations of molecularly targeted agents, targeting mTOR, PI3K, PTEN, ATRX, NF1 or DDR. Treatment of the GBM-PDOs in our 4D arrays allowed the identification of possibly effective combination therapies. Moreover, our results suggest that targeted therapy against multiple pathways simultaneously, at least *in vitro* in the 3D GBM-PDOs, may be more advantageous than monotherapy, although this would need to be tested more rigorously. Recent studies utilizing PDC cultures could predict resistance to EGFR inhibitors and test the repurposing of ibrutinib for EGFR-specific therapy in GBM (Lee et al., 2018). Also, PDOs from gastrointestinal cancers could recapitulate patient responses in clinical trials of personalized medicine (Vlachogiannis et al., 2018). Our studies utilizing GBM-PDOs revealed that niraparib (targeting DDR) and BEZ235 (targeting PI3K/mTOR) could act synergistically, whereas BEZ235 may protect from TMZ toxicity, therefore substantiating another recent report on utilizing PDOs for initiating PI3K/mTOR-targeting therapy in a patient with GBM (Loong et al., 2020) and providing new inroads for combination therapy. Further validations of the synergistic effects *in vivo*, tailoring combinations against clonal cell subpopulations for each GBM, and including other combinations, e.g., with immune checkpoint inhibitors could support future clinical translation. Intriguingly, we identified synergistic activities at lower-than-expected growth inhibitory drug concentrations, therefore suggesting that our 4D printing approach provides a platform to identify potential thresholds for combination therapy to spare the dose-limiting toxicities in GBM (Mehta et al., 2015). In addition, our platform incorporated the assessment of on-target activity offering a validation strategy for personalized therapy (Bartucci et al., 2016; Loong et al., 2020; Vlachogiannis et al., 2018). We generated a 4D platform using SMP that self-transforms from 3D arrays, for PDO culture, into histological cassettes for rapid assessment of drug sensitivity, on-target activity, and synergy. When including exome and/or single-cell sequencing, and histological and targeted therapy assays, we propose that this system could potentially be used for evaluation of therapeutic responses in future PMO clinical trials.

Limitations of the Study

This platform is not without limitations. First, we utilized Matrigel droplets as an ECM source for PDOs. Variability among animal-derived or chemically defined synthetic ECMs could confound the cellular responses in drug testing. Second, culture conditions and growth factor components might limit the prolonged preservation of TME components. Although these stromal components, such as immune, endothelial, and nerve cells, may be reintroduced in coculture to reproduce the natural tissue architecture, modeling of their native architecture and precise bidirectional communication with tumor cells are key for modeling tumor heterogeneity and predicting drug sensitivity. Third, biomechanical variables and bioactive molecules may be reproduced by using biomaterials or bionics. Our future improvements will integrate the SMP 4D printing with different PDOs and TME, ECM bioinks, microfluidics, and/or ALI conditions to provide more precise monitoring of tumor multicellular and clonal interactions and assess metabolic responses to therapy at the native tissue level. Fourth, we utilized GBM PDOs for drug responses after 2 weeks of culture eying the rapid assessment in a time frame that could be feasible for clinical therapeutic decision making. Additional studies are needed to determine the extent of changes in drug responses when allowing PDOs to produce more complex connections and to study the contribution of cellular TME components toward generating full (organ)-mimicking organoids while exploiting the key differences between GBM- and ESC/iPSC-derived organoids. Finally, further research and more patient samples will be required to assure the clinical application and scaling of the developed assay. Improving on these limitations in future studies will allow the discovery of novel therapeutics that may be assessed in PMO clinical trials and used to select more effective personalized therapies.

Resource Availability

Lead Contact

Further information and requests for resources and reagents should be directed to and will be fulfilled by the lead contact, Hatem E. Sabaawy (sabaawhe@cinj.rutgers.edu).

Materials Availability

All unique/stable reagents generated in this study are available from the lead contact with a completed materials transfer agreement.

Data and Code Availability

The published article includes all datasets generated or analyzed during this study.

METHODS

All methods can be found in the accompanying Transparent Methods supplemental file.

SUPPLEMENTAL INFORMATION

Supplemental Information can be found online at https://doi.org/10.1016/j.isci.2020.101365.

ACKNOWLEDGMENTS

We thank our patients for consenting to donating their tissues for use in our studies. We thank Rutgers Cancer Institute of New Jersey Biorepository Services and Tissue Analytical Services (Shafiq Bhat, Lucyann Franciosa, Kelly Walton, and Lei Cong) for assistance with tissue acquisition, histology, immunohistochemistry, and sample processing. We also thank Diane Hanahan and Dr. Parisa Javidian for access to the tissue banking protocols and clinical assessments. We thank Sohan Ganguli and Christopher Ragusa for their help on prototyping of the biaxial stretching device.

This project was supported in part with Federal funds from the National Cancer Institute (NCI), National Institutes of Health (NIH), under Contract No. HHSN2612008000001E (to H.E.S.); NCI R01 award (CA226746 to H.E.S.); Rutgers Cancer Institute of New Jersey Shared Resources, supported, in part, with funding from NCI-CCSG (P30CA072720); and New Jersey Health Foundation Innovation Award (ISFP 7-16 to H.E.S.). The content of this publication does not necessarily reflect the views or policies of the Department of Health and Human Services, nor does mention of trade names, commercial products, or organizations imply endorsement by the U.S. Government. We thank Dr. Ralph Parchment of Division of Cancer Treatment and Diagnosis Laboratory, Frederick National Laboratory for Cancer Research sponsored by NCI, for discussion throughout this project.

AUTHOR CONTRIBUTIONS

H.L. and H.E.S. conceived the study. C.Y. and H.L. designed, fabricated and tested the self-transformation of the cell-culture insert array. M.C., L.L., C.M.G., and K.J. performed the PDS and PDO experiments. M.C., L.Q., C.M.G., K.J., and H.E.S. analyzed the data, H.E.S. wrote the manuscript, and all authors contributed to editing the manuscript.

DECLARATION OF INTERESTS

Rutgers University has filed two patent applications (PCT/US2018/039994 and PCT/US2019/029931) on the methods described in the manuscript. H.E.S. is the scientific founder of Celvive, Inc.

Received: December 2, 2019
Revised: April 29, 2020
Accepted: July 8, 2020
Published: August 21, 2020

REFERENCES

Bansal, N., Bartucci, M., Yusuff, S., Davis, S., Flaherty, K., Huselid, E., Patrizii, M., Jones, D., Cao, L., Sydorenko, N., et al. (2016). BMI-1 targeting interferes with patient-derived tumor-initiating cell survival and tumor growth in prostate cancer. Clin. Cancer Res. *22*, 6176–6191.

Barthel, F.P., Johnson, K.C., Varn, F.S., Moskalik, A.D., Tanner, G., Kocakavuk, E., Anderson, K.J., Abiola, O., Aldape, K., Alfaro, K.D., et al. (2019). Longitudinal molecular trajectories of diffuse glioma in adults. Nature *576*, 112–120.

Bartucci, M., Ferrari, A.C., Kim, I.Y., Ploss, A., Yarmush, M., and Sabaawy, H.E. (2016). Personalized medicine approaches in prostate cancer employing patient derived 3D organoids and humanized mice. Front. Cell Dev. Biol. *4*, 64.

Bartucci, M., Hussein, M.S., Huselid, E., Flaherty, K., Patrizii, M., Laddha, S.V., Kui, C., Bigos, R.A., Gilleran, J.A., El Ansary, M.M.S., et al. (2017). Synthesis and characterization of novel BMI1 inhibitors targeting cellular self-renewal in hepatocellular carcinoma. Target Oncol. *12*, 449–462.

Bian, S., Repic, M., Guo, Z., Kavirayani, A., Burkard, T., Bagley, J.A., Krauditsch, C., and Knoblich, J.A. (2018). Genetically engineered cerebral organoids model brain tumor formation. Nat. Methods *15*, 631–639.

Eiraku, M., Watanabe, K., Matsuo-Takasaki, M., Kawada, M., Yonemura, S., Matsumura, M., Wataya, T., Nishiyama, A., Muguruma, K., and Sasai, Y. (2008). Self-organized formation of polarized cortical tissues from ESCs and its active manipulation by extrinsic signals. Cell Stem Cell *3*, 519–532.

Ge, Q., Sakhaei, A.H., Lee, H., Dunn, C.K., Fang, N.X., and Dunn, M.L. (2016). Multimaterial 4D printing with tailorable shape memory polymers. Sci. Rep. *6*, 31110.

Gimple, R.C., Bhargava, S., Dixit, D., and Rich, J.N. (2019). Glioblastoma stem cells: lessons from the tumor hierarchy in a lethal cancer. Genes Dev. *33*, 591–609.

Hubert, C.G., Rivera, M., Spangler, L.C., Wu, Q., Mack, S.C., Prager, B.C., Couce, M., McLendon, R.E., Sloan, A.E., and Rich, J.N. (2016). A three-dimensional organoid culture system derived from human glioblastomas recapitulates the hypoxic gradients and cancer stem cell heterogeneity of tumors found in vivo. Cancer Res. *76*, 2465–2477.

Ianevski, A., He, L., Aittokallio, T., and Tang, J. (2017). SynergyFinder: a web application for analyzing drug combination dose-response matrix data. Bioinformatics *33*, 2413–2415.

Jacob, F., Salinas, R.D., Zhang, D.Y., Nguyen, P.T.T., Schnoll, J.G., Wong, S.Z.H., Thokala, R., Sheikh, S., Saxena, D., Prokop, S., et al. (2020). A patient-derived glioblastoma organoid model and biobank recapitulates inter- and intra-tumoral heterogeneity. Cell *180*, 188–204.e22.

Jin, X., Kim, L.J.Y., Wu, Q., Wallace, L.C., Prager, B.C., Sanvoranart, T., Gimple, R.C., Wang, X., Mack, S.C., Miller, T.E., et al. (2017). Targeting glioma stem cells through combined BMI1 and EZH2 inhibition. Nat. Med. *23*, 1352–1361.

Lancaster, M.A., Renner, M., Martin, C.A., Wenzel, D., Bicknell, L.S., Hurles, M.E., Homfray, T., Penninger, J.M., Jackson, A.P., and Knoblich, J.A. (2013). Cerebral organoids model human brain development and microcephaly. Nature *501*, 373–379.

Lee, H., and Cho, D.W. (2016). One-step fabrication of an organ-on-a-chip with spatial heterogeneity using a 3D bioprinting technology. Lab Chip *16*, 2618–2625.

Lee, J.K., Liu, Z., Sa, J.K., Shin, S., Wang, J., Bordyuh, M., Cho, H.J., Elliott, O., Chu, T., Choi, S.W., et al. (2018). Pharmacogenomic landscape of patient-derived tumor cells informs precision oncology therapy. Nat. Genet. *50*, 1399–1411.

Linkous, A., Balamatsias, D., Snuderl, M., Edwards, L., Miyaguchi, K., Milner, T., Reich, B., Cohen-Gould, L., Storaska, A., Nakayama, Y., et al. (2019). Modeling patient-derived glioblastoma with cerebral organoids. Cell Rep. *26*, 3203–3211.e5.

Loong, H.H., Wong, A.M., Chan, D.T., Cheung, M.S., Chow, C., Ding, X., Chan, A.K., Johnston, P.A., Lau, J.Y., Poon, W.S., et al. (2020). Patient-derived tumor organoid predicts drugs response in glioblastoma: a step forward in personalized cancer therapy? J. Clin. Neurosci. *20*, S0967–S5868.

Mehta, M., Khan, A., Danish, S., Haffty, B.G., and Sabaawy, H.E. (2015). Radiosensitization of primary human glioblastoma stem-like cells with low-dose AKT inhibition. Mol. Cancer Ther. *14*, 1171–1180.

Mirani, B., Pagan, E., Shojaei, S., Duchscherer, J., Toyota, B.D., Ghavami, S., and Akbari, M. (2019). A 3D bioprinted hydrogel mesh loaded with all-trans retinoic acid for treatment of glioblastoma. Eur. J. Pharmacol. *854*, 201–212.

Neal, J.T., Li, X., Zhu, J., Giangarra, V., Grzeskowiak, C.L., Ju, J., Liu, I.H., Chiou, S.H., Salahudeen, A.A., Smith, A.R., et al. (2018). Organoid modeling of the tumor immune microenvironment. Cell *175*, 1972–1988.e16.

Neftel, C., Laffy, J., Filbin, M.G., Hara, T., Shore, M.E., Rahme, G.J., Richman, A.R., Silverbush, D., Shaw, M.L., Hebert, C.M., et al. (2019). An integrative model of cellular states, plasticity, and genetics for glioblastoma. Cell *178*, 835–849.e21.

Nikiforova, M.N., Wald, A.I., Melan, M.A., Roy, S., Zhong, S., Hamilton, R.L., Lieberman, F.S., Drappatz, J., Amankulor, N.M., Pollack, I.F., et al. (2016). Targeted next-generation sequencing panel (GlioSeq) provides comprehensive genetic profiling of central nervous system tumors. Neuro Oncol. *18*, 379–387.

Ogawa, J., Pao, G.M., Shokhirev, M.N., and Verma, I.M. (2018). Glioblastoma model using human cerebral organoids. Cell Rep. *23*, 1220–1229.

Parker, R.N., Cairns, D.M., Wu, W.A., Jordan, K., Guo, C., Huang, W., Martin-Moldes, Z., and Kaplan, D.L. (2020). Smart material hydrogel transfer devices fabricated with stimuli-responsive silk-elastin-like proteins. Adv. Healthc. Mater. *9*, e2000266.

Pasca, A.M., Sloan, S.A., Clarke, L.E., Tian, Y., Makinson, C.D., Huber, N., Kim, C.H., Park, J.Y., O'Rourke, N.A., Nguyen, K.D., et al. (2015). Functional cortical neurons and astrocytes from human pluripotent stem cells in 3D culture. Nat. Methods *12*, 671–678.

Patel, A.P., Tirosh, I., Trombetta, J.J., Shalek, A.K., Gillespie, S.M., Wakimoto, H., Cahill, D.P., Nahed, B.V., Curry, W.T., Martuza, R.L., et al. (2014). Single-cell RNA-seq highlights intratumoral heterogeneity in primary glioblastoma. Science *344*, 1396–1401.

Patrizii, M., Bartucci, M., Pine, S.R., and Sabaawy, H.E. (2018). Utility of glioblastoma patient-derived orthotopic xenografts in drug discovery and personalized therapy. Front. Oncol. *8*, 23.

Prados, M.D., Byron, S.A., Tran, N.L., Phillips, J.J., Molinaro, A.M., Ligon, K.L., Wen, P.Y., Kuhn, J.G., Mellinghoff, I.K., de Groot, J.F., et al. (2015). Toward precision medicine in glioblastoma: the promise and the challenges. Neuro Oncol. *17*, 1051–1063.

Rajakulendran, N., Rowland, K.J., Selvadurai, H.J., Ahmadi, M., Park, N.I., Naumenko, S., Dolma, S., Ward, R.J., So, M., Lee, L., et al. (2019). Wnt and Notch signaling govern self-renewal and differentiation in a subset of human glioblastoma stem cells. Genes Dev. *33*, 498–510.

Reynolds, B.A., and Weiss, S. (1992). Generation of neurons and astrocytes from isolated cells of the adult mammalian central nervous system. Science *255*, 1707–1710.

Rodon, J., Soria, J.C., Berger, R., Miller, W.H., Rubin, E., Kugel, A., Tsimberidou, A., Saintigny, P., Ackerstein, A., Brana, I., et al. (2019). Genomic and transcriptomic profiling expands precision cancer medicine: the WINTHER trial. Nat. Med. *25*, 751–758.

Rokita, J.L., Rathi, K.S., Cardenas, M.F., Upton, K.A., Jayaseelan, J., Cross, K.L., Pfeil, J., Egolf, L.E., Way, G.P., Farrel, A., et al. (2019). Genomic profiling of childhood tumor patient-derived xenograft models to enable rational clinical trial design. Cell Rep. *29*, 1675–1689.e9.

Sabaawy, H.E. (2013). Genetic heterogeneity and clonal evolution of tumor cells and their impact on precision cancer medicine. J. Leuk. *1*, 1000124.

Sicklick, J.K., Kato, S., Okamura, R., Schwaederle, M., Hahn, M.E., Williams, C.B., De, P., Krie, A., Piccioni, D.E., Miller, V.A., et al. (2019). Molecular profiling of cancer patients enables personalized combination therapy: the I-PREDICT study. Nat. Med. *25*, 744–750.

Siegel, R.L., Miller, K.D., and Jemal, A. (2020). Cancer statistics, 2020. CA Cancer J. Clin. *70*, 7–30.

Tuveson, D., and Clevers, H. (2019). Cancer modeling meets human organoid technology. Science *364*, 952–955.

Vinci, M., Burford, A., Molinari, V., Kessler, K., Popov, S., Clarke, M., Taylor, K.R., Pemberton, H.N., Lord, C.J., Gutteridge, A., et al. (2018). Functional diversity and cooperativity between subclonal populations of pediatric glioblastoma and diffuse intrinsic pontine glioma cells. Nat. Med. *24*, 1204–1215.

Vlachogiannis, G., Hedayat, S., Vatsiou, A., Jamin, Y., Fernandez-Mateos, J., Khan, K., Lampis, A., Eason, K., Huntingford, I., Burke, R., et al. (2018). Patient-derived organoids model treatment response of metastatic gastrointestinal cancers. Science *359*, 920–926.

Weller, M., Wick, W., Aldape, K., Brada, M., Berger, M., Pfister, S.M., Nishikawa, R., Rosenthal, M., Wen, P.Y., Stupp, R., et al. (2015). Glioma. Nat. Rev. Dis. Primers *1*, 15017.

Yang, C., Boorugu, M., Dopp, A., Ren, J., Martin, R., Han, D., Choi, W., and Lee, H. (2019). 4D printing reconfigurable, deployable and mechanically tunable metamaterials. Mater. Horiz. *6*, 1244–1250.

Yi, H.G., Jeong, Y.H., Kim, Y., Choi, Y.J., Moon, H.E., Park, S.H., Kang, K.S., Bae, M., Jang, J., Youn, H., et al. (2019). A bioprinted human-glioblastoma-on-a-chip for the identification of patient-specific responses to chemoradiotherapy. Nat. Biomed. Eng. *3*, 509–519.

Zheng, X., Deotte, J., Alonso, M.P., Farquar, G.R., Weisgraber, T.H., Gemberling, S., Lee, H., Fang, N., and Spadaccini, C.M. (2012). Design and optimization of a light-emitting diode projection micro-stereolithography three-dimensional manufacturing system. Rev. Sci. Instr. *83*, 125001.

iScience, Volume *23*

Supplemental Information

Rapid Processing and Drug Evaluation in Glioblastoma Patient-Derived Organoid Models with 4D Bioprinted Arrays

Michelle Chadwick, Chen Yang, Liqiong Liu, Christian Moya Gamboa, Kelly Jara, Howon Lee, and Hatem E. Sabaawy

SUPPLEMENTAL DATA:

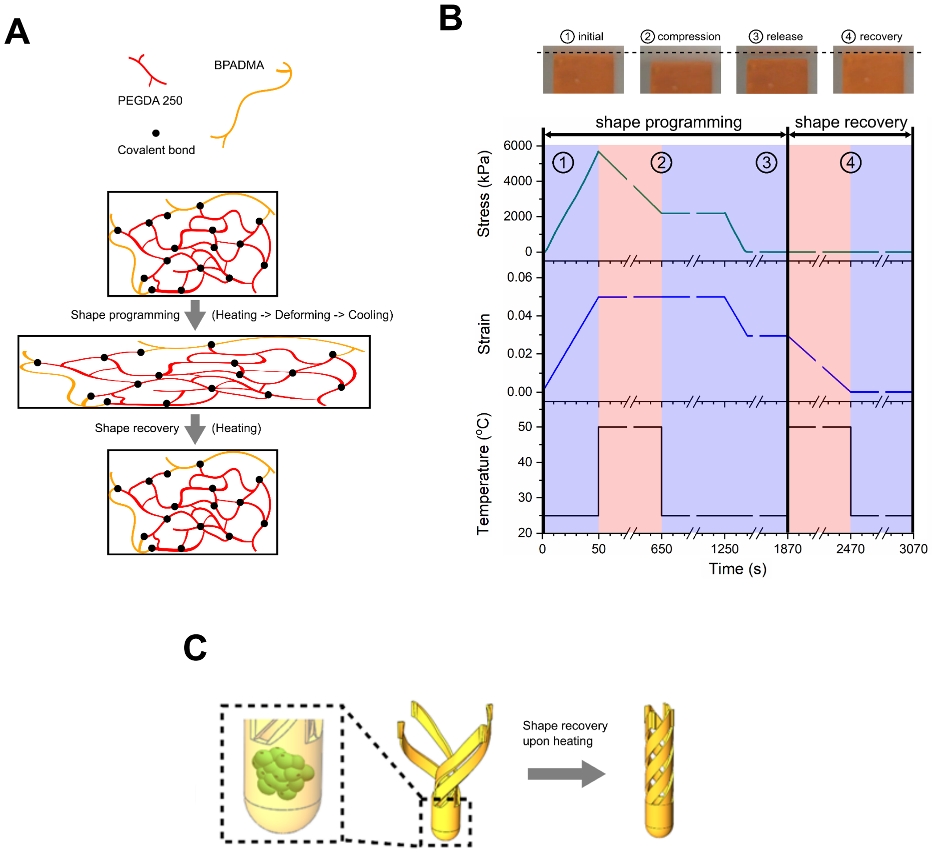

Figure S1. Shape memory effect of the shape memory polymer utilized to generate the 4D printed cell-culture insert arrays. Related to Figure 1. (A) A schematic showing the SMP materials PEGDA 250 and BPADMA used to manufacture the cell-culture insert array by forming cross-linked polymeric network. These SMP interconnect through covalent bonds created during photopolymerization. During shape programming, the temperature was first raised to mobilize polymer chains for deforming the polymer network, while covalent bonds remain unchanged. Since mobility of polymer chains decreases at low temperature, the deformed shape can be temporarily fixed. When heated, the polymer chains become mobilized again, restoring its original thermodynamic- favored shape without any external stress. (B) A diagram showing the thermodynamic features of the SMP. A beam was compressed by 5% at 25°C. While maintaining the strain, the beam was heated to 50°C and then cooled down to 25°C again. Note that the required stress to maintain the compressive strain was significantly reduced due to fixing of the deformed shape. After removal of the mechanical loading, the deformed strain was retained at 3%. Upon heating back to 50°C, the original height of the beam could be completely recovered. (C) A diagram demonstrating the design advantage of the array with a lower cell compartment protecting the biological materials from external stresses. The lower cell compartment of a representative well from the cell-culture insert array harboring inside the biological material (e.g. PDOs), while the large deformation enabling the shape transformation to occur in the upper helical bridges. When heating is applied, PDO cells have already undergone fixation with formaldehyde. Therefore, no distortion due to external stress or heating was noticeable when using the arrays.

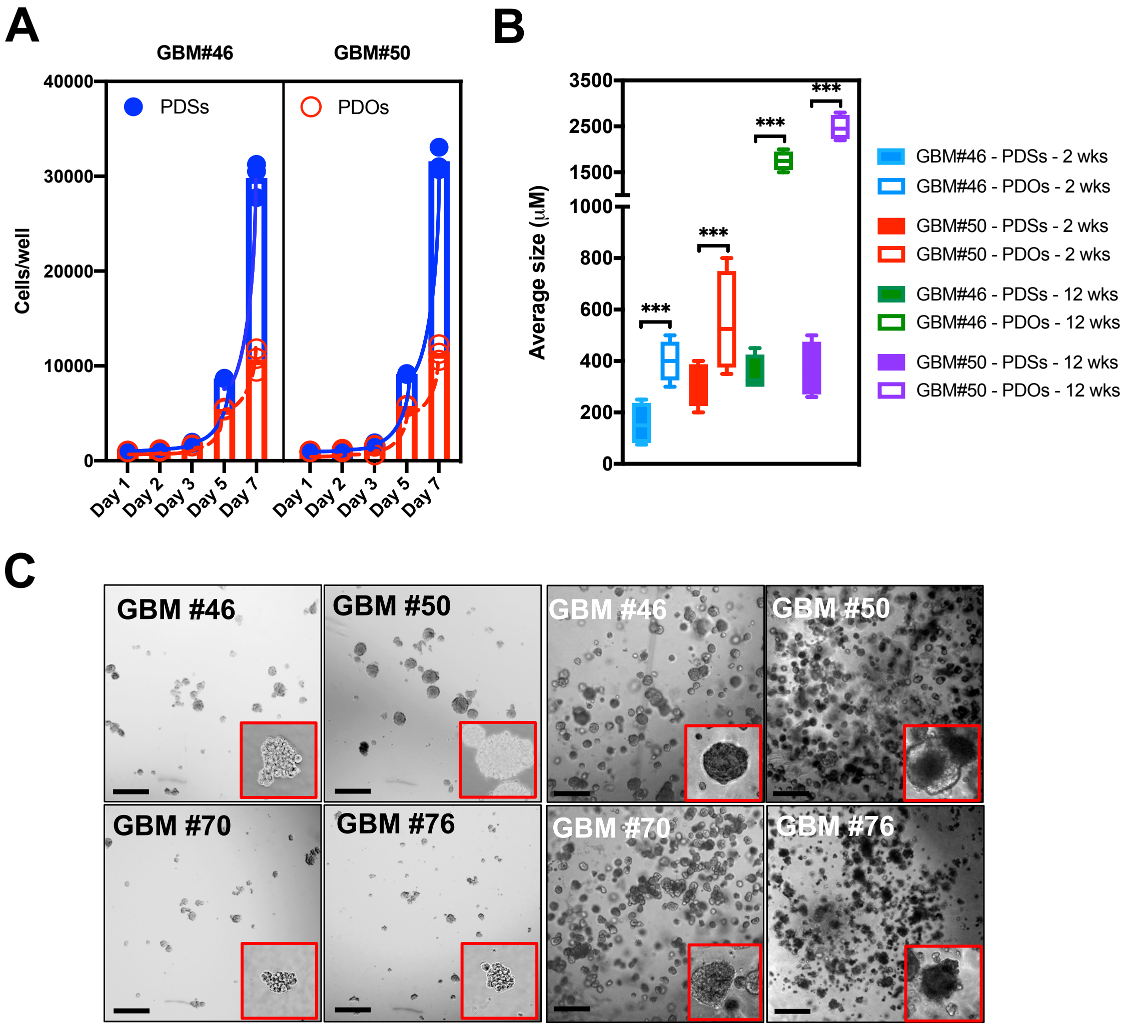

Figure S2. Features of GBM-PDO cells. Related to Figure 2. (A) Cell counts per well during the first 7 days of GBM-PDS and -PDO cultures. PDSs were rapidly proliferating between days 3-7 much faster than PDOs. After day 7, GBM-PDOs continued to grow and were significantly bigger at day 14 and up to 12 weeks in culture. (B) Average size of GBM-PDSs and -PDOs based on microscopic and image J analysis. (C) Bright field images of 3D cultured GBM-PDSs (left) and -PDOs (right) after 12 weeks of culture. Comparison between PDSs vs PDOs in (A and B) are represented as mean ± S.D. of 4 replicates and significance was determined by one-way ANOVA (***p<0.001).

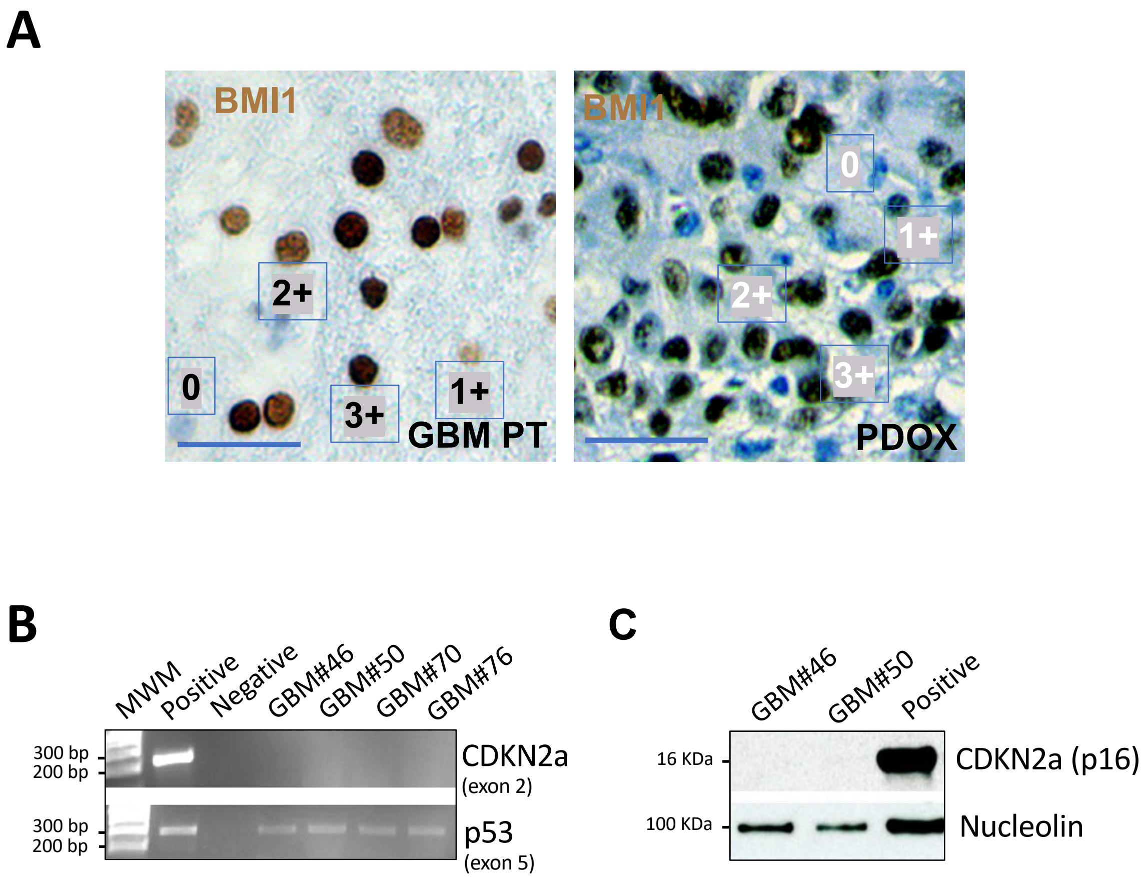

Figure S3. BMI1, CDKN2a and p53 levels assessment in GBM patients and models. Related to Figures 4 and 5. (A) Representative IHC images of BMI1 expression in the originating GBM#46 and their derived mouse PDOX. Scoring of cells with representative BMI1 level (0-3+) is demonstrated next to each corresponding representative cell. Images were quantified for the amount of BMI1 positive staining, as well as for intensity of the staining. H scores were calculated as (% at 0) * 0 + (% at 1+) * 1 + (% at 2+) * 2 + (% at 3+) * 3 = Range 0 – 300 based on analyses of at least 10 fields per slide averaged by two qualified examiners. H scores were 148±12 for GBM#46 and averaged 132±22 from 4 PDOXs derived from GBM#46. (B) PCR amplification of genomic DNA from GBM#46, GBM#50, GBM#70 and GBM#76 revealed that exon 2 of the CDKN2A locus, which is shared between both $p16^{INK4a}$ and $p14^{ARF}$, failed to amplify when compared to genomic DNA from HEK293T cells (positive), while amplification of PCR products corresponding to exon 5 of TP53 (p53, exon 5) could be detected from these GBMs. MWM, molecular weight marker. These data, together with the Glioseq data, suggested that cells from these four GBMs have homozygous CDKN2a losses. (C) The genomic data of CDKN2a homozygous losses were confirmed at the protein level from the GBMs with available tissues when compared to HEK293T cells, there was no detectable CDKN2a (p16) expression at the expected size (16 KDa), even after over-exposure of lysates from the positive control. Nucleolin levels were used as nuclear/loading controls with an observed band size of 100 KDa. Data represent three independent experiments.

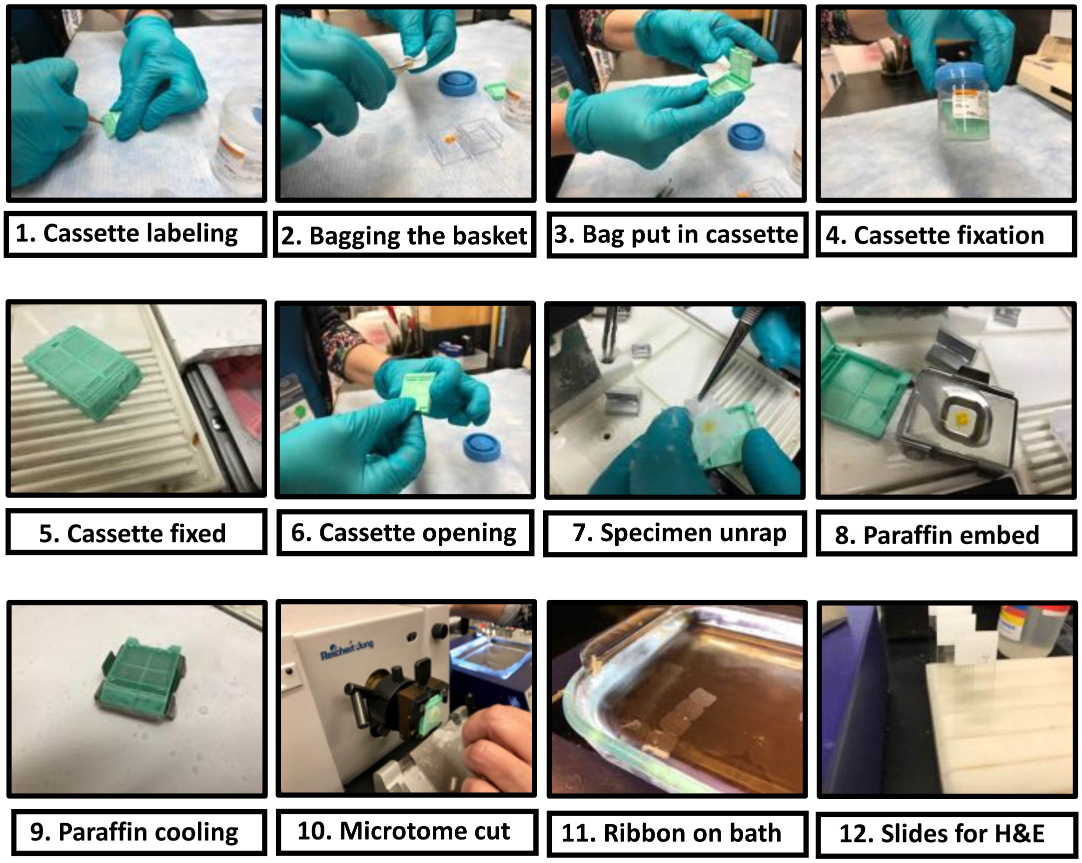
1. Cassette labeling
2. Bagging the basket
3. Bag put in cassette
4. Cassette fixation
5. Cassette fixed
6. Cassette opening
7. Specimen unrap
8. Paraffin embed
9. Paraffin cooling
10. Microtome cut
11. Ribbon on bath
12. Slides for H&E

Images of histological processing steps

Figure S4. Histological processing steps of 4D cell-culture insert arrays. Related to Figures 1 and 4. Demonstration of the twelve steps used in the manual histological processing of the biospecimen in the cell-culture insert arrays. Automatic histological processing has also been examined and SMP cell-culture insert arrays were compatible with the automated processing.

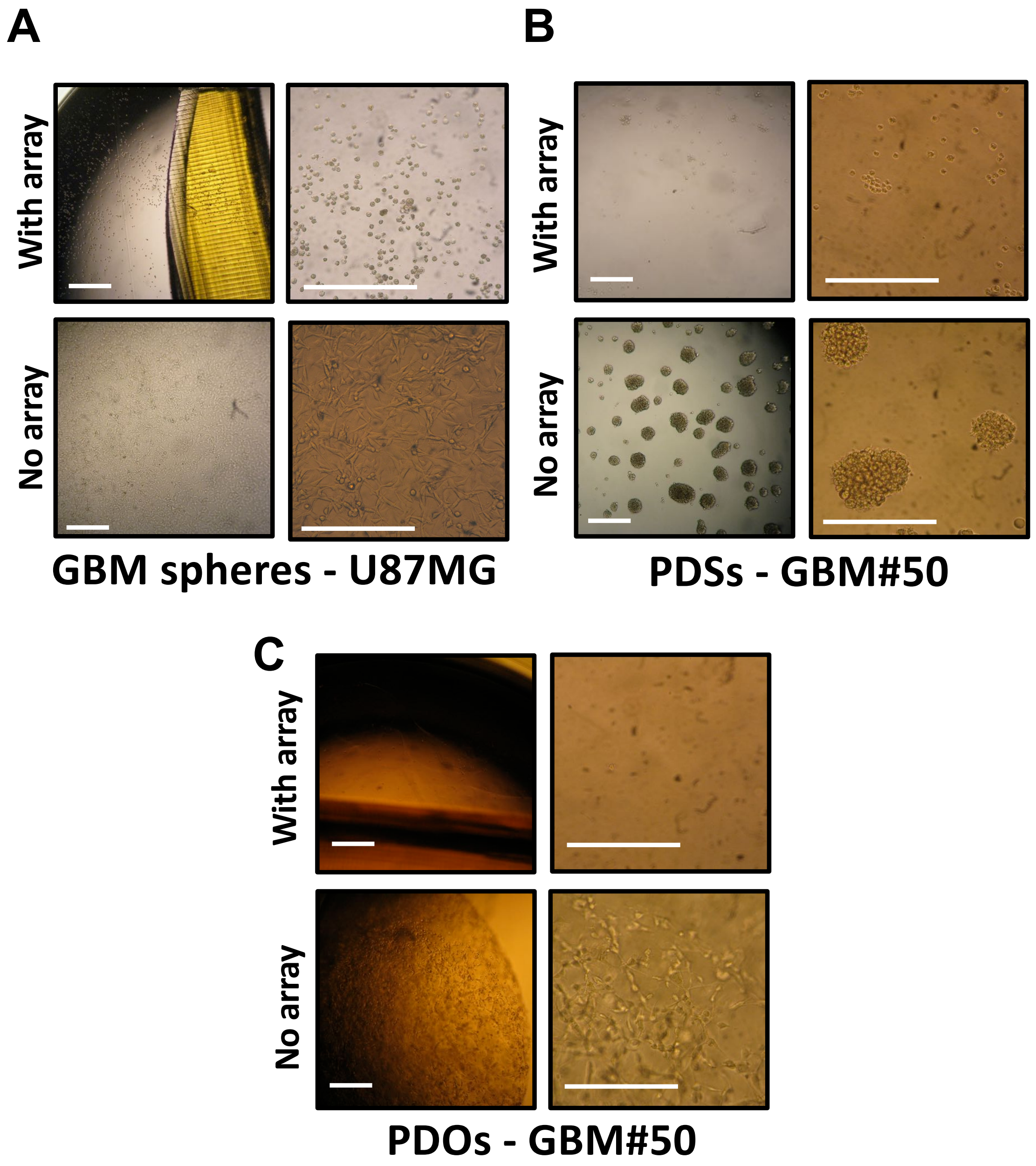

Figure S5. Biocompatibility of the 4D printed cell-culture insert arrays. Related to Figures 1 and 4. (A) Examination of GBM U87MG cells cultured in sphere culture conditions and GBM#50 PDS and PDO cultures with or without the 4D SMP arrays. (B) Images of 3D cultured GBM#50 PDSs with or without the 4D SMP arrays. (C) Images of 3D cultured GBM#50 PDOs with or without the 4D SMP arrays. Scale bars in (A-C) are 100 μm.

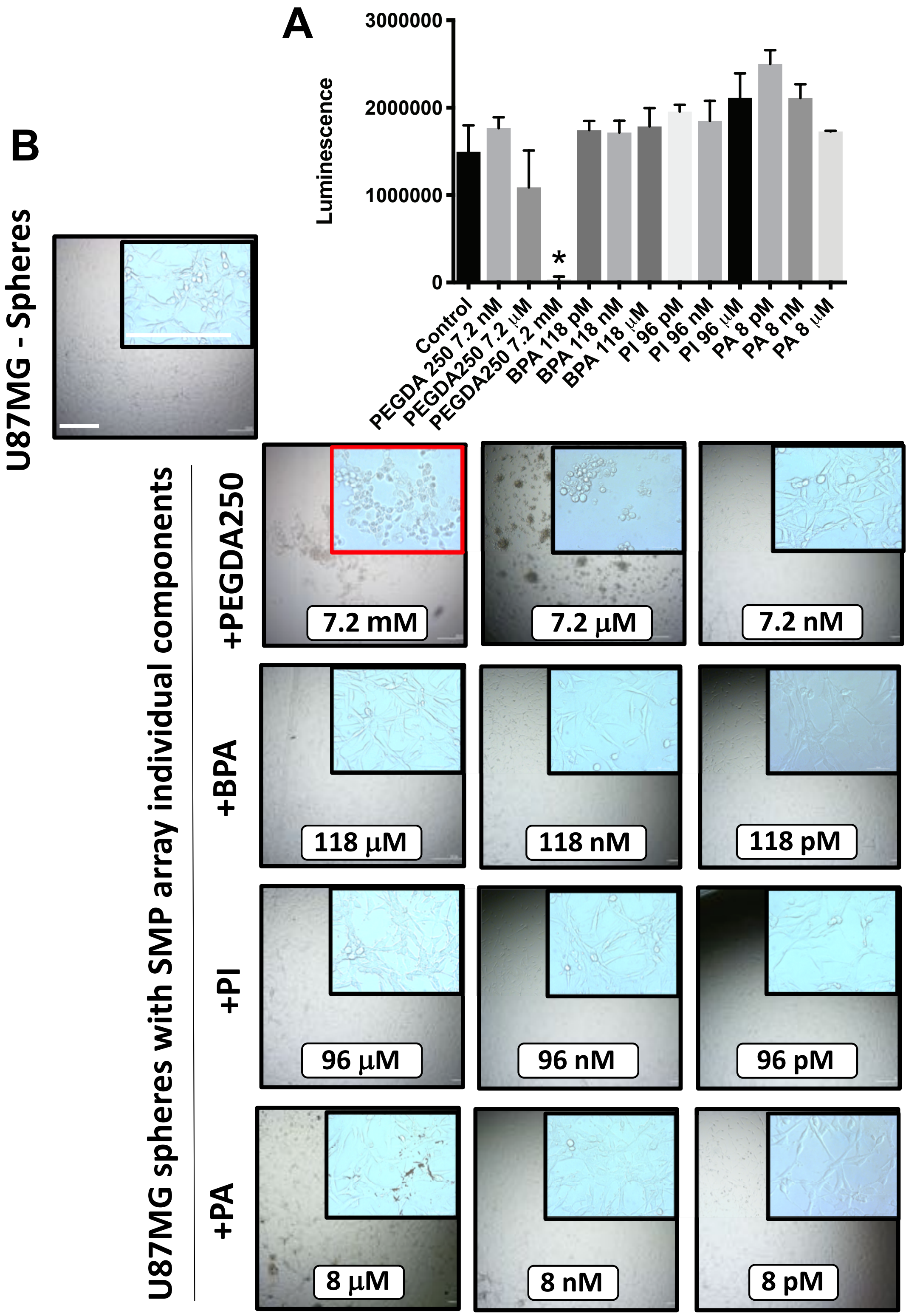

Figure S6. Components of additive manufacturing for generating the 4D printed cell-culture insert arrays are tested for effects on GBM sphere formation. Related to Figures 1 and 4. (A) Cell viability of U87MG cells cultured in sphere conditions for one week in the presence of each chemical component used for the 4D printing and additive manufacturing of the SMP array. Testing for each component was performed over a 2Log concentrations. and displayed at concentrations ranging from mM to pM for each chemical. (B) Representative bright field images of U87MG cells in sphere culture conditions for one week in the presence of individual components of the SMP chemicals at the indicated conc. Insets are higher power (20X) magnification of the 5x images. Luminescence effects of different chemicals are represented as mean ± S.D. of three replicates and significance was determined by student t test (*$p<0.05$). Only PEGDA250 when used at 7.2 mM (1,000 times higher concentration than the 7.2 μM concentration used for manufacturing the SMP) induced a significant reduction in cell viability (red inset). Scale bars in control image on the left and all treatment images are 100 μm.

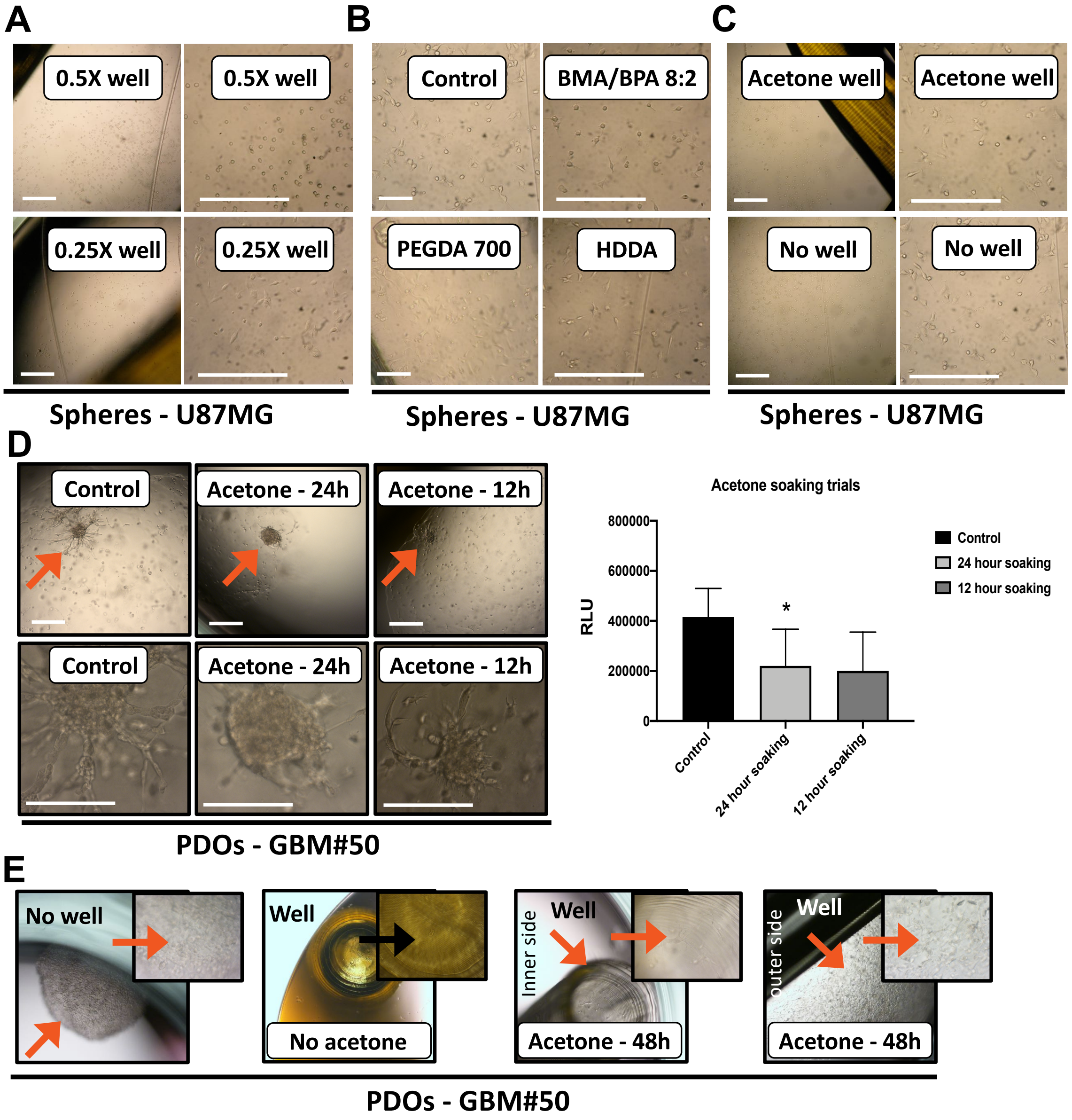

Figure S7. Acetone soaking allowed the use of 4D printed cell-culture insert arrays for GBM sphere and organoid long-term culture. Related to Figures 1 and 4. (A) PDS culture with individual well components of arrays in 3D sphere culture conditions for one week. (B) Images of sphere culture with selected components of the SMP and 4D printing chemicals that were individually examined at the final concentrations used in the prototype array to define the conditions that allowed normal sphere culture. (C) Images showing that incubation of 4D printed insert array wells in 100% acetone bath after 3D printing allows normal sphere culture. (D) GBM-PDO culture upon soak trials for 12-24 hour in acetone gradually improved 3D cultures. Data are represented as mean ± S.D. of four replicates and comparisons between acetone soaking trials and control were assessed by student t test (*$p<0.05$) and determined that at least 24-hour of acetone bath soaking is required. (E) Incubation of 4D printed cell-culture insert arrays in 100% acetone bath after 3D printing for 5 days was finally determined to allow normal GBM organoid-like culture. Bright field images showing organoid-like growth within the insert array upon soaking in 100% acetone bath for 5 days after 3D printing (red arrows, images showing comparable growth to the no array well control at 48 hours), compared to no organoid growth when an acetone bath was not used (no acetone, black arrow). Panels on the right are higher magnifications of the images on the left in (A, C and E) and panels on the bottom are higher magnifications of the images on the top in (D). Scale bars in (A-D) are 100 μm.

TRANSPARENT METHODS

Materials

All chemicals including both liquid oligomers, photoinitiator (PI) and photo absorber (PA) were purchased from Sigma-Aldrich (St. Louis, MO, USA). For 3D printing, poly(ethylene glycol) diacrylate (PEGDA) (Mn250) and Bisphenol A ethoxylate dimethacrylate (BPADMA) (Mn 1700) were used. Phenylbis(2,4,6-trimethylbenzoyl) phosphine as PI and Sudan I as PA were used to initiate polymerization and control UV light penetration, respectively.

Processing of 4D printed cell-culture insert arrays

4D printing refers to 3D prints with smart materials that is responsive to external stimuli (Yang et al., 2019). Key elements for generating the 4D printed arrays included determining the 3D printability, 3D shapes between which self-transformation occurs (a cell-culture insert array and a histology mega-cassette), PI and PA properties and thermo-stimulus properties. The smart material utilized in this study was a shape memory polymer (SMP), and the high precision 3D printing technique was projection micro-stereolithography (PμSL) (Yang et al., 2019; Zheng et al., 2012). SMPs were fixed in a temporarily deformed shape and restored to the original shape upon heating around glass transition temperature (T_g) (Yang et al., 2019; Zheng et al., 2012). Mathematical modeling may predict the transition and final state of 4D printed constructs (Ashammakhi et al., 2018). Mathematical modeling was performed to assess the outcome of multiple printing processes and determine the state of printed materials upon applying different stimuli (Lee laboratory, unpublished data). 3D printed cell-culture insert arrays were rinsed four times in fresh ethanol for 30 second each to remove non-crosslinked precursor solution. After air drying, the inserts were rinsed in pentane and post-cured in a UV oven (UVP, 365 nm) for 2 hours. To eliminate toxicity from any residual 3D printing material, the inserts were soaked in an acetone bath for 5 days, rinsed in ethanol and PBS for sterilization and dried overnight at room temperature (RT).

Operation of 4D printed culture inserts

For operating the culture insert, at RT, an insert in the cassette configuration was first mounted on a custom-built stretcher. The insert was stretched to 96-well plate configuration at RT. After rotation, both the insert and the stretcher were placed in an oven at 50°C for 20 minute and then cooled down to RT to program the stretched shape. The insert was then mounted onto a fixture and a 96-well plate. Cells and culture media were injected into each well using micropipette. After cell culture, the insert was removed from the fixture and heated to 50°C to induce shape recovery to the cassette configuration while maintaining the registry of the cultured cells. In the cassette configuration, the insert was ready for histological processing to obtain the histology of the entire 4D printed culture inserts.

Quantitative RT-PCR

We performed GBM subtype gene signatures and gene expression profiling using a subset of markers based on TCGA database and signatures associated with tumor histology, grade and defining molecular features (Jin et al., 2017). For Quantitative RT-PCR, total RNA was isolated with the RNeasy kit (Qiagen) and reverse-transcribed into cDNA using the aScript cDNA SuperMix (Quanta Biosciences). Real-time PCR was performed on an Applied Biosystems StepOne Plus cycler using SYBR-green Mastermix (Thermo Scientific). Expression values were normalized to 18S.

Patient derived 3D cell culture

To generate patient-derived 3D cell culture, patient samples were obtained from patients undergoing resection at Robert Wood Johnson University Hospital under an Institutional Review Board approved protocol. GBM tissues were processed mechanically by cutting into small pieces (<1mm) and were incubated in serum-free media (Advanced DMEM F12 (Gibco, REF #12634-010)with primocin (InvivoGen, ant-pm-1), B27 (Gibco, REF #12587-001), EGF (PeproTech, #AF-100-15-100UG) and FGF (PeproTech, #AF-100-18B-500UG) at 20 ng/mL). They were then incubated with Accutase at 37°C for 2-4 minute and passed through a needle to obtain single cell suspension. Cells were plated in the serum-free media on ultra-low attachment plates (Grenier, #655185) and treatments were done in these 96-well plates. PDSs were utilized for clonogenic assays by allowing limiting dilution of GBM cells to form gliospheres, defined as clusters of greater than 50 cells and larger than 50 μm in diameter, for 7 days. Every two days, half of the media were replaced and gliopheres were counted. Single cells from day-7 gliospheres were used in secondary and tertiary gliosphere assays (Mehta et al., 2015), and the sphere forming potentials were determined (Bansal et al., 2016). The organoid forming potential data were similarly determined from day-14 GBM-PDOs. Data were analyzed using ELDA software (http://bioinf.wehi.edu.au/software/elda/).

Generation, imaging and analysis of 3D GBM-PDOs

To generate patient-derived organoids, cells grown in serum-free media were mixed at 10^3 cells/well of a 96-well plate in 20% media and 80% Matrigel (Corning, REF# 356237). From this initial mix, 10 μL were injected per well of the 4D printed culture inserts using a microinjection p20 pipette. The 4D printed culture inserts were placed at 37°C for one hour. After this hour, 300 μL of organoid media was added per well (Neurobasal media (Gibco, REF #21103-049), B27 (-Vitamin A), sodium pyruvate (Himedia, TCL015-100ML), hydrocortisone (1 mM), EGF and FGF at 20 ng/mL). Media for PDO cultures were partially (~80%) replaced three times per week and 3D cultures were performed between one week to 12 weeks. In some cases, organoid cultures were transferred to bioreactors under similar conditions (Lancaster et al., 2013), and only after 2 weeks of 3D plate cultures to reduce the development of organoid central necrotic cores. These organoids in the bioreactor tended to fuse into larger organoids when cultures were extended for 12 weeks and were not considered for drug testing assays. In an organotypic migration and invasion model, GBM-PDO cell migration from within the matrigel droplets to the plate or culture insert surface and invasion of the surrounding matrigel droplets in three-dimensional matrices were captured with phase contrast using the IncuCyte HDs system. Frames were captured at 4-hour intervals from time 0 to 72 hour from 2 separate regions/well using a x10 objective. Image processing involved fluorescent color-channel separation, data resizing, illumination adjustment and threshold setting and data extraction for each GBM-PDO.

Immunofluorescence (IF), WB and IHC

IF and IHC titration of antibodies and basic conditions were established (Kramer et al., 2013; Patel et al., 2012), and modified to adapt to 3D culture models and for using with the cell-culture insert arrays. Organoid-like cultures within the 96- or 24-well plates without the array or within the 96- or 6-well plates with the array were fixed for 10 minutes at 37°C with 4% paraformaldehyde followed by 3 washes with PBS. For IF, they were permeabilized overnight at 4°C with 0.5% Triton X-100 in PBS followed by 3 washes with PBS. Primary antibody was incubated at RT overnight followed by 3 washes in PBS. Secondary antibody with phalloidin (Life Technologies, REF#

A12380, 1:200) and DAPI (Invitrogen, REF# D1306, 1:200) were incubated overnight at RT followed by 3 washes in PBS. Images were taken on a Nikon A1R Si confocal microscope. For IHC, following fixation, the organoids were taken to pathology where they were processed and embedded in paraffin. They were then sectioned at a thickness of 5 μM. They were then stained using the Ventana Discovery XT automated IHC instrument. For phospho S6 assays, PTEN status in GBMs or GBM-PDOs were determined against control PTEN-proficient and -deficient GBM tissues to establish phospho S6 expression detection levels (Baeza et al., 2003). Antibodies were used against these targets: BMI1 (CST, #6964, 1:200), GALC (Santa Cruz Biotechnology, sc-67352, 1:100), GFAP (Cell Signaling Technologies (CST, #3670, 1:200), phospho S6 (CST, #2215, 1:50), NESTIN (Millipore, #MAB5326, 1:50), SOX2 (CST, #23064, 1:400), TLX (Invitrogen, #PA5-40484, 1:100), and TUJ1 (Millipore, #MAB1637, 1:100). Antibodies used for WB were for: p16 (2D9A12) (Santa Cruz Biotechnology, sc-81157, 1:1,000) and Nucleolin (Abcam, #ab22758, 1:1,000).

Generation of mouse PDOX

Mice were anesthetized with 100 mg/kg Ketamine (Henry Schein, NDC 11695-0702-1) and 10 mg/kg Xylazine (Akorn, NDC 59399-110-20) in PBS. The scalp was shaved, and the mouse immobilized within a stereotactic device. An incision was made to expose the bregma. A small hole was created based on the bregma- X: 2.5 mm right and Y: 1.5 mm anterior using a drill. A Hamilton syringe was used to inject 3-8 X 10^4 GBM cells in 4 μl over 7.5 minutes at 3.5 mm deep at stereotaxic coordinates of 1 mm posterior to the bregma and +2 mm mediolateral from the midline. The syringe was slowly removed over 3 minutes and bone wax used to seal the hole. The incision was then closed with surgical glue. The coordinates for stereotactic implantation were chosen based on pilot studies to result in generating a laterally positioned tumor within the cerebral hemisphere while avoiding injury to the thalamus and avoiding the seeding of the cerebrospinal fluid with tumor cells that may give rise to undesirable spinal tumors or ulcerating tumors into the orbit. To create PDOX using GBM-PDOs, a similar protocol was used with a few differences. GBM-PDOs were first dissociated into a single cell suspension using a protocol initially developed for primary bone marrow cells (Kokorina et al., 2012) and modified using the manufacturer's protocol (BD Cell Recovery Solution, #354253). The cells were then resuspended at 30,000 cells in 3 μL media. These cells were then orthotopically injected at a rate of 0.5 μL/minute. These mice were monitored until they reached 3 months post-injection, at which point MRI was performed, demonstrating GBM tumor formation. Mouse brains were collected for histological assessment of PDOX tumor formation with H&E and IHC staining.

Effects of 4D printed culture inserts on cell viability

To determine how the culture inserts affected cell growth, cells were plated in the presence of varying concentrations of each of the individual components. Cells used included PDSs, PDOs, and U87MG cells. U87MG cells were grown in MEM (Gibco, REF #11090-081) with 1% pen/strep (Gibco, REF #15140-122) and 10% FBS (Sigma, F4135-500ML). Calculations for the concentrations were determined using the % volume of each component used in the inserts. A 10% of that was used to account for potential leaching effects. Cells were plated at 1,000 cells/condition. Cell viability was measured using the Promega Cell Titer Glo assay (Promega, REF #G7572). Cell viability was also assessed after plating with different sizes of the insert material and 4D printed culture insert material soaked for 5 days in acetone.

We first established optimum seeding densities for 3D cultures by determining the clonal efficiencies of deriving 3D cultures from dissociated patient cells at limiting dilutions to single cells

(Bansal et al., 2014; Vinci et al., 2012) to test the cell-culture insert arrays. Following seeding in the 4D printed culture inserts, GBM-PDOs were allowed to grow for 2 weeks. After 2 weeks, the media was aspirated from each well and replaced with media containing the treatment drug. Growth inhibitory conc. at 50% (GI_{50}) conc. were determined for each drug, compared to untreated and DMSO-treated organoid cells. Temozolomide (TMZ) (Sigma, T2577) was used at a GI_{50} at 100 μM, BEZ-235 (Selleck, S1009) at 1 μM, and Niraparib (Selleck, S7625) at 4 nM. Cells were incubated at 37°C for 72 hours. Synergy screens consisted of dose response matrices ranging from 1X to 0.1X of the GI_{50} conc. for each drug. Isobologram for calculation and visualization of synergy scores from reduced GBM cell proliferation measured by ATP levels and synergistic response of the Bliss score surface observed using the combination of TMZ plus BEZ235 or niraparib plus BEZ235 were generated using the SynergyFinder application (Ianevski et al., 2017).

Manual and automated histological processing of the 4D printed culture inserts

After drug treatments, culture inserts were fixed in a dish containing PFA for 2 hours at RT. The dish was then moved to 50°C for 20 minutes to allow the cell-culture inserts to shrink. Inserts were then placed inside a cassette and taken to pathology for processing. Briefly, Cell-culture insert arrays underwent dehydration followed by embedding in a paraffin block. These blocks were then cut in 5 μm sections using a microtome.

Statistical analyses

Data were normalized to the standard (Control). Analysis of significance was performed by two-way ANOVA with Bonferroni post-hoc test for comparing treatment effects and by Student's *t*-test when only two groups were compared using GraphPad Prism 8. Unless otherwise indicated, all experiments were performed at least thrice; *n* refers to biological replicates.

SUPPLEMENTAL REFERENCES:

Ashammakhi, N., Ahadian, S., Zengjie, F., Suthiwanich, K., Lorestani, F., Orive, G., Ostrovidov, S., and Khademhosseini, A. (2018). Advances and Future Perspectives in 4D Bioprinting. Biotechnol J *13*, e1800148.

Baeza, N., Weller, M., Yonekawa, Y., Kleihues, P., and Ohgaki, H. (2003). PTEN methylation and expression in glioblastomas. Acta neuropathologica *106*, 479-485.

Bansal, N., Davis, S., Tereshchenko, I., Budak-Alpdogan, T., Zhong, H., Stein, M.N., Kim, I.Y., Dipaola, R.S., Bertino, J.R., and Sabaawy, H.E. (2014). Enrichment of human prostate cancer cells with tumor initiating properties in mouse and zebrafish xenografts by differential adhesion. Prostate *74*, 187-200.

Kokorina, N.A., Granier, C.J., Zakharkin, S.O., Davis, S., Rabson, A.B., and Sabaawy, H.E. (2012). PDCD2 knockdown inhibits erythroid but not megakaryocytic lineage differentiation of human hematopoietic stem/progenitor cells. Exp Hematol *40*, 1028-1042 e1023.

Kramer, J., Granier, C.J., Davis, S., Piso, K., Hand, J., Rabson, A.B., and Sabaawy, H.E. (2013). PDCD2 controls hematopoietic stem cell differentiation during development. Stem Cells Dev *22*, 58-72.

Patel, N., Klassert, T.E., Greco, S.J., Patel, S.A., Munoz, J.L., Reddy, B.Y., Bryan, M., Campbell, N., Kokorina, N., Sabaawy, H.E., *et al*. (2012). Developmental regulation of TAC1 in peptidergic-induced human mesenchymal stem cells: implication for spinal cord injury in zebrafish. Stem Cells Dev *21*, 308-320.

Vinci, M., Gowan, S., Boxall, F., Patterson, L., Zimmermann, M., Court, W., Lomas, C., Mendiola, M., Hardisson, D., and Eccles, S.A. (2012). Advances in establishment and analysis of three-dimensional tumor spheroid-based functional assays for target validation and drug evaluation. BMC Biol *10*, 29.